Improved experimental limit on the electric dipole moment of the electron

Eugene D. Commins, Stephen B. Ross,* David DeMille, and B. C. Regan
Physics Department, University of California, Berkeley, California 94720
and Lawrence Berkeley Laboratory, University of California, Berkeley, California 94720
(Received 10 May 1994)

New results are reported in our search for the electric dipole moment d_e of the electron in the ground $6\,^2P_{1/2}$ state of ^{205}Tl. The atomic-beam magnetic resonance method is employed with separated oscillating fields. A magnetic field **B** defines the axis of quantization, and an electric field **E**, parallel to **B**, is applied in the region between the oscillating fields. Laser optical pumping is used for state selection and analysis, and the signal is fluorescence accompanying the decay of excited atoms in the analyzer region. The signature of a nonzero electric dipole moment is a dependence of the signal on the P,T-odd rotational invariant $\mathbf{E}\cdot\mathbf{B}$ (P and T denote parity and time reversal, respectively). Two counterpropagating atomic beams are employed to reduce a systematic effect due to the motional magnetic field $\mathbf{E}\times\mathbf{v}/c$. Auxiliary experiments are performed to isolate and eliminate residual sources of systematic error. The result is $d_e=[1.8\pm1.2(\text{statistical})\pm1.0(\text{systematic})]\times10^{-27}$ e cm. A detailed discussion is given of the experimental method, sources of systematic error and their elimination, and results.

PACS number(s): 35.10.Di, 14.60.Cd, 11.30.Er, 42.50.Wm

I. INTRODUCTION

In this paper we report results in our search for the electric dipole moment (EDM) of the electron [1,2]. Existence of an EDM would imply that time-reversal (T) invariance and parity (P) are violated. Searches for the EDM of the electron [3–6], the neutron [7,8], and nuclear EDM's [9,10] are motivated by the existence of charge-parity (CP) violation in neutral kaon decay, which is known to be equivalent to T violation [11]. No satisfactory theoretical explanation for CP violation exists, but several theoretical models of that phenomenon have been proposed (see Table I), with widely varying predictions for the electron EDM [12–15]. According to the standard model, the electron EDM is far too small to be detected, but a number of plausible alternative models predict values for the electron EDM large enough to be observed in practical experiments.

To detect the presence of an electric dipole moment **d**, one must place the particle of interest in an electric field **E** and measure its incremental energy: $W=-\mathbf{d}\cdot\mathbf{E}$. In the case of the free (neutral) neutron, this can be done directly, but it is obviously impossible for a free (charged) electron. One is thus led to the following question: If an unpaired valence electron in a neutral paramagnetic atom were to possess an EDM $\mathbf{d}_e$, would the atom as a whole possess an EDM $\mathbf{d}_a$ proportional to $\mathbf{d}_e$? At first glance this would appear to be impossible, since a neutral atom is not accelerated when placed in a uniform external electric field. Thus, the average force on each of the charges in the atom must be zero. Since in the nonrelativistic limit, the force on a charge is proportional to the local electric field, this would seem to imply that the average electric field at each charge in the atom is zero. The external **E** field would, therefore, be screened by rearrangement (polarization) of the other charges.

However, this simple argument, which may be cast in quantum mechanical form [16], is valid only in the nonrelativistic limit. Sandars [17] has demonstrated that when relativistic effects are taken into account, $\mathbf{d}_a$ can actually

TABLE I. Summary of theoretical predictions for the electron EDM from Refs. [15] and references therein.

CP violation model	Prediction
Standard model	$\lvert d_e\rvert < 10^{-38}$ e cm
Supersymmetric models	$\lvert d_e\rvert \leq 10^{-27}$ e cm
Left-right symmetric models	$\lvert d_e\rvert$ in range 10^{-26} to 10^{-28} e cm
Higgs models	$\lvert d_e\rvert$ in range 10^{-28} to 3×10^{-27} e cm
Lepton flavor-changing models	10^{-29} e cm $\leq \lvert d_e\rvert \leq 10^{-26}$ e cm

*Present address: Max Planck Institute for Quantum Optics, Hans Kopfermann-Strasse 1, D-85748, Garching, Germany.

TABLE II. Calculated enhancement factors.

Atom	Atomic no.	State	Enhancement factor	Ref.
Li	3	$2\,^2S_{1/2}$	0.004	[27]
Na	11	$3\,^2S_{1/2}$	0.33	[27]
K	19	$4\,^2S_{1/2}$	3.0	[27]
Rb	37	$5\,^2S_{1/2}$	27	[27,28]
Cs	55	$6\,^2S_{1/2}$	114	[28,29]
Fr	87	$7\,^2S_{1/2}$	1150	[17]
Tl	81	$6\,^2P_{1/2}$	−585	[18]
Xe	54	$^3P_2$	130	[5]
Au	79	$6\,^2S_{1/2}$	≈250[a]	[28]
Hg	80	$^1S_0$	−0.014	[30]

[a]Uncertain.

be quite large for suitable paramagnetic atoms. The ratio $R=\mathbf{d}_a/\mathbf{d}_e$ is found to be $\approx Z^3\alpha^2$ in magnitude (where Z is the atomic number and α is the fine structure constant). The "enhancement factor" R has by now been calculated quite accurately for a number of atoms by a variety of many-electron relativistic perturbation techniques (see Table II). For the ground $6\,^2P_{1/2}$ state of thallium ($Z=81$), one finds

$$R=-585 \tag{1}$$

with a theoretical uncertainty of about 5% [18]. In the present experiment, a search is made for $\mathbf{d}_a(^{205}\mathrm{Tl};6\,^2P_{1/2})$ and the results are interpreted in terms of $\mathbf{d}_e$ by means of (1).

It should be noted that in principle a finite $\mathbf{d}_a$ could arise from a variety of causes: (a) an intrinsic nucleon EDM, (b) a P,T-odd nucleon-nucleon interaction, (c) an intrinsic electron EDM, or (d) a P,T-odd electron-nucleon interaction [19]. The present experiment is not sensitive to (a) or (b) but is sensitive primarily to (c). However, our results may also be used to place a limit on one form of (d), and to set useful limits on possible P-even, T-odd e-e, and e-N interactions, as well as T-odd beta decay couplings [20].

II. EXPERIMENTAL METHOD

A. Brief sketch of the method

We first give a brief and simplified description of the experiment. The atomic-beam magnetic resonance method with separated oscillating fields [21] is employed (see Fig. 1). The experiment is performed in a weak uniform magnetic field **B** that defines the axis of quantization z; (typically $B_Z=0.42$ G). A strong electric field **E** (typically 107 kV/cm) is placed between the two oscillating field regions and is nominally parallel to **B**. In order to minimize an important possible systematic effect (the "E×v" effect), we utilize two counterpropagating beams of atomic Tl, which are emitted from their sources and travel in the $\pm x$ directions (vertical to minimize the effects of gravity).

Let us follow the up-going beam in order to explain the main features. As the beam emerges from the oven, it consists almost entirely of atoms in an incoherent mixture of the ground state components $F=1$, $m_F=+1,0,-1$ and $F=0$, $m_F=0$, with essentially equal populations. (See Fig. 2 for the energy levels of ^{205}Tl.) In the state selector, the atomic-beam intersects a laser beam propagating in the y direction, linearly polarized in the z direction, and tuned to the $E1$ transition $6P_{1/2}$, $F=1\rightarrow 7S$, $F=1$ at 378 nm (see Fig. 3). Here the selection rule $\Delta m_F=0$ holds; moreover there is no transition $F=1$, $m_F=0\rightarrow F=1$, $m_F=0$, since the corresponding

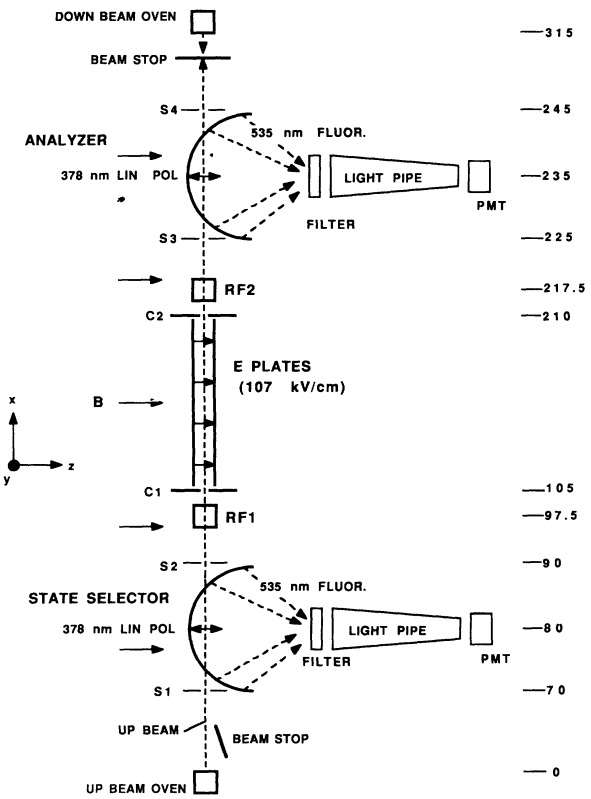

FIG. 1. Schematic diagram of experimental apparatus. $S1$–4 and $C1,2$ are slits referred to in text. Numbers at right refer to distances in centimeters from the up-beam oven slit to $S1$, center of state selector, etc.

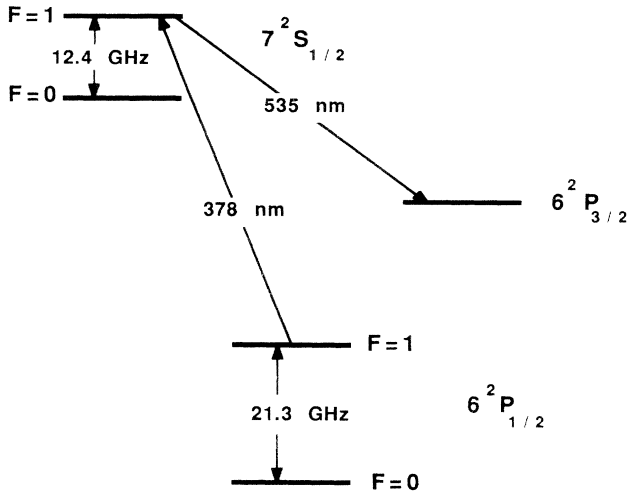

FIG. 2. Low-lying energy levels of ^{205}Tl, not to scale.

Clebsch-Gordan coefficient is zero. Atoms excited to the $7S$, $F=1$, $m_F=\pm1$ states decay spontaneously in the following ways: (a) to $6P_{1/2}$, $F=1$, $m_F=\pm1$ states, from which they are repumped, (b) to $6P_{1/2}$, $F=1$, $m_F=0$, where they remain, (c) to $6P_{1/2}$, $F=0$, $m_F=0$, where they remain and play no further role, or (d) to the metastable state $6P_{3/2}$, accompanied by fluorescence at 535 nm, which is detected. Since the mean life of $6P_{3/2}$ (≈ 0.2 s) is long compared to the transit time of the beam through the apparatus, atoms arriving in this state remain and play no further role.

Consequently, as the beam emerges from the state selector region, the $6P_{1/2}$, $F=1$ level contains only atoms in the $m_F=0$ sublevel, the $m_F=\pm1$ components having been depopulated. We may represent the $F=1$ state by the three-component spinor

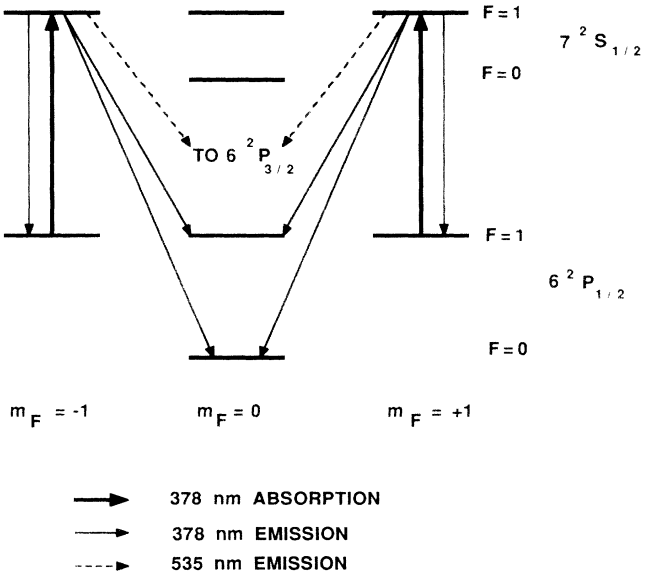

FIG. 3. Schematic diagram for optical pumping of the transition $6\,^2P_{1/2}$, $F=1\rightarrow 7\,^2S_{1/2}$, $F=1$ at 378 nm.

$$\psi=\begin{pmatrix}0\\1\\0\end{pmatrix}. \tag{2}$$

The beam next traverses the first rf region (RF1 in Fig. 1) of length $l=5$ cm. Here a magnetic field $B_1\cos(\omega t)\hat{\mathbf{x}}$ oscillates in the x direction at frequency ω tuned to the $M1$ transitions $6P_{1/2}$, $F=1$, $m_F=0\rightarrow m_F=\pm1$. (Note that for $B_z=0.4$ G, the shift in frequency of the $m_F=0$ state due to its dependence on B_z^2 is less than 2 Hz.) On resonance, for a monoenergetic atomic beam, and for the appropriate field magnitude B_1, ψ undergoes the following transformation in RF1:

$$\psi\rightarrow\psi'=\frac{-i}{\sqrt{2}}\begin{pmatrix}1\\0\\1\end{pmatrix}, \tag{3}$$

here expressed in the rotating frame. Thus, as the $F=1$ atoms emerge from RF1, they are in a coherent superposition of $m_F=\pm1$ components.

The beam then passes through the electric field E of length $L=100$ cm. If $d_a\neq0$, ψ' undergoes the following transformation:

$$\psi'\rightarrow\psi''=\frac{-i}{\sqrt{2}}\begin{pmatrix}\exp(-i\eta_E\varepsilon)\\0\\\exp(i\eta_E\varepsilon)\end{pmatrix}\approx\frac{-i}{\sqrt{2}}\begin{pmatrix}(1-i\eta_E\varepsilon)\\0\\(1+i\eta_E\varepsilon)\end{pmatrix}, \tag{4}$$

where $\eta_E=\pm1$ for $E>0$, $E<0$, respectively, and

$$\varepsilon=\frac{-d_a|E|}{\hbar}\frac{L}{v}=\frac{-d_eR|E|}{\hbar}\frac{L}{v}, \tag{5}$$

where v is the beam velocity.

The beam next passes through the second rf region RF2, also of length $l=5$ cm. RF2 contains magnetic field $B_1\cos(\omega t+\alpha)\hat{\mathbf{x}}$, which oscillates coherently with that of RF1 and has the same amplitude, but differs from the latter by a phase $\alpha=\pm\pi/4$ or $\pm3\pi/4$. On resonance and for $\alpha=\pm\pi/4$, ψ'' undergoes the following transformation in RF2 in the rotating frame:

$$\psi''\rightarrow\psi'''=\begin{pmatrix}\pm\eta_B e^{-i\eta_B\alpha}\dfrac{(1\mp\eta_E\eta_B\varepsilon)}{2}\\-\dfrac{1}{\sqrt{2}}(1\pm\eta_E\eta_B\varepsilon)\\\mp\eta_B e^{i\eta_B\alpha}\dfrac{(1\mp\eta_E\eta_B\varepsilon)}{2}\end{pmatrix}, \tag{6}$$

and where $\eta_B=\pm1$ for $B_z>0$, $B_z<0$, respectively.

Finally, the atoms enter the analyzer region. Here a second laser beam, directed as before along the y axis, with z linear polarization, and tuned to the transition $6P_{1/2}$, $F=1\rightarrow 7S$, $F=1$ at 378 nm, intersects the atomic beam. Once again optical pumping occurs, and only atoms in the states $6P_{1/2}$, $F=1$, $m_F=\pm1$ are excited to the $7S$ state. The fluorescence at 535 nm accompanying decay of $7S$ atoms in the analyzer region is detected. Its

intensity is proportional to the sum of the populations of $6P_{1/2}$, $F=1$, $m_F=\pm 1$ states just prior to laser excitation; hence, from (6) it is proportional to

$$S=|1\mp\eta_E\eta_B\varepsilon|^2\approx 1\mp 2\eta_E\eta_B\varepsilon\ . \tag{7}$$

By observing the change in S when E or B are reversed, one measures ε and thus d_e. In (7), the term with ε is proportional to the P,T-odd pseudoscalar $\mathbf{E}\cdot\mathbf{B}$.

By means of automatically controlled beam stops, we switch back and forth periodically from the up beam to the down beam. The state selector, RF1, RF2, and the analyzer for the up beam become the analyzer, RF2, RF1, and the state selector, respectively, for the down beam.

For the beam velocities and electric fields employed in this experiment, an electron EDM of 1×10^{-27} e cm (where e is the electronic charge) would correspond to $|\varepsilon|\approx 3\times10^{-7}$. Thus, to reach a sensitivity of 1×10^{-27} e cm, we must measure an asymmetry of several parts in 10^7. Quite clearly this requires careful attention to systematic effects and the acquisition of much data.

In the idealized description just given, we have ignored a number of important features, including the beam velocity distributions, the deviation of applied radio frequency from resonance, the quadratic Stark effect, the $\mathbf{E}\times\mathbf{v}$ effect, and a geometric phase effect. In the sections that follow, these features are introduced as we discuss various aspects of the experiment in detail.

B. The atomic beams

The atomic-beam ovens, of conventional design [22], are made of 304 stainless steel and equipped with 0.05-cm-diam helically wound tantalum wire heaters supported in ceramic insulators. A full oven load consists of about 130 g of 99.999% pure thallium metal with natural abundance: 70% $A=205$, 30% $A=203$. For each oven the source slit is 0.95 cm deep (x), 0.95 cm long (y), and 0.125 cm wide (z). The oven reservoir and slit regions have separately controlled heaters to maintain the slit jaws at slightly higher temperatures than the reservoir; this prevents condensation of thallium on the jaws. Typical reservoir operating temperatures are $\approx$920 K, at which the vapor pressure of Tl is approximately 0.04 torr, and the fluxes of atoms from the up-beam and down-beam source slits are $F\approx 9\times10^{16}$ s^{-1} and 5×10^{16} s^{-1}, respectively. (These differ because of details in oven construction.) For the fluxes stated, one oven load lasts for months of operation. Much higher fluxes ($\approx 8\times10^{17}$ s^{-1}) have been generated at temperatures up to 1080 K. It would be appropriate to employ such fluxes if noise in the signal were dominated by shot noise; however, this is not the case, and at present, very little improvement in noise is obtained by operating the ovens above 920 K.

The velocity distribution of each atomic beam is approximated by the standard formula

$$f(v)=\frac{2}{v_0^4}v^3\exp\left[-\left[\frac{v}{v_0}\right]^2\right], \tag{8}$$

where $v_0=\sqrt{2kT_{\text{eff}}/M}$. T_{eff} is expected to be considerably higher than 920° because of the large depth of the source slits [23]. In fact we find from measurements of the width of magnetic resonance "Ramsey" fringes (see Sec. II F) that $T_{\text{eff}}\approx 1090$ K, which corresponds to $v_0=3.0\times10^4$ cm s^{-1} and an average beam velocity $\langle v\rangle=1.33\ v_0=3.9\times10^4$ cm s^{-1}. Direct measurements of the velocity distribution were carried out by rapidly switching the polarization of state selector and analyzer laser beams with the aid of Pockels cells. The results are in agreement with (8) but the precision of these measurements is not very high.

Each oven is mounted on a double translation stage controlled by micrometer screws from outside the vacuum system, for translation in the y and z directions. Each atomic beam passes through a sequence of slits (see Fig. 1). Slit assemblies 1,2,3,4 are mounted on translation stages that permit motion in the z direction, controlled from outside the vacuum. For normal operation slits 1, 2, 3, and 4 are centered on the beam axis and are 1.0 cm long (y) and 0.1 cm wide (z); ("full" slits). However, a variety of other choices are possible (see Fig. 4). The inclined slit shown in Fig. 4 is useful for determining the sensitivity of the detectors as a function of atom position in the y direction, while the full and half slits are useful for auxiliary measurements of contributions to the $\mathbf{E}\times\mathbf{v}$ effect (see Sec. III A). The collimating slits C_1,C_2 are mounted on fixtures attached to the electric field plate assembly, and are aligned with respect to the electric field plates on the bench, prior to insertion in the vacuum system. These slits are 0.5 cm long (y) and 0.05 cm wide (z). In normal operation, the beam dimensions are defined by the collimating slits and the relevant source slit, not slits 1–4, which are large enough to be cleared by the beams. The distances in the x direction of slits 1–4 and C_1,C_2 from each source are given in Fig. 1.

C. Optical pumping

The 378-nm light is generated by a Coherent CR 699-21 ring dye laser, pumped by red light (typically 5.3 W) from a Coherent 100 K 3 krypton laser. The ring laser utilizes LD 700 dye to produce single mode 756-nm radi-

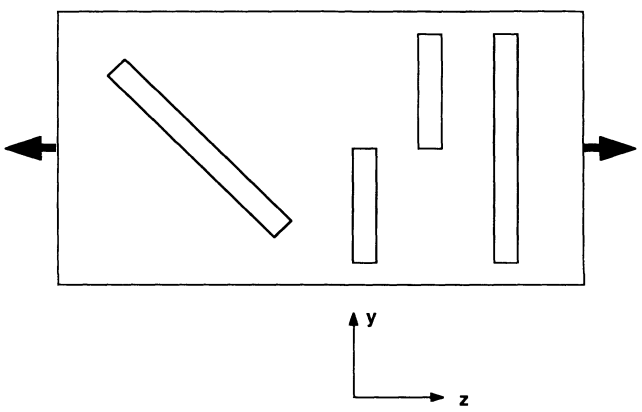

FIG. 4. Arrangement of slits, $S1-4$. The assembly can be translated in z, as indicated by arrows.

ation, and a $LiIO_3$ doubling crystal mounted inside the ring cavity is employed to generate 378-nm photons. Typically, we extract a 378-nm beam with a power of ≈ 3 mW and a bandwidth of ≈ 1 MHz.

The state selector and analyzer each consist of an ellipsoidal mirror of polished aluminum, with the intersection (interaction region) of the atomic and laser beams at the near focus, the axis of symmetry along z, and the semimajor and minor axes equal to 14.6 and 9.8 cm, respectively. The reflectivity for 535-nm radiation over a wide range of angles is better than 85%. An optical filter is located close to the other focal point. It is a 7.6-cm-diam colored glass filter (Hoya Y44) that transmits 535 nm but absorbs 378-nm light. On the surface of the filter facing the interaction region there is a coating with reflectivity $\geq 99.5\%$ for 378 nm at all incident angles $\leq 45°$, and with 85% transmission of 535-nm light. The filter is followed by a 60-cm-long tapered plastic light pipe with 70% transmission for 535 photons, at the end of which is placed an Amperex XP 3461B photomultiplier tube. The 68-mm-diam photocathode is of the green-extended bialkali type with $\approx 14\%$ quantum efficiency at 535 nm. The overall efficiency of this system for light collection and photoelectric conversion is $\approx 5\%$.

Figure 5 shows typical optical pumping signals obtained on the transition $6P_{1/2}, F=1 \rightarrow 7S, F=1$ for ^{205}Tl, with no rf fields applied. (The ^{205}Tl optical resonance is separated from the corresponding resonance in ^{203}Tl by the isotope shift: 1.55 GHz.) Both state selector and analyzer fluorescent signals shown in Fig. 5 are power-broadened considerably compared to the natural width of 21 MHz. In addition, the analyzer signal is finite on the wings of the resonance but dips to zero over an extended region near resonance center. This occurs because the population of $6P_{1/2}, F=1, m_F=\pm 1$ atoms is reduced to zero in the state selector at optical resonance, and is not replenished in the space between state selector and analyzer unless rf-induced reorientation occurs. Detailed calculations yield optical pumping curves in good quantitative agreement with the observations of Fig. 5. During data acquisition, the laser frequency may drift slowly. To recenter it, we periodically generate optical resonances such as are shown in Fig. 5, use a computer algorithm to find the center of the state selector resonance curve, and correct the laser frequency accordingly.

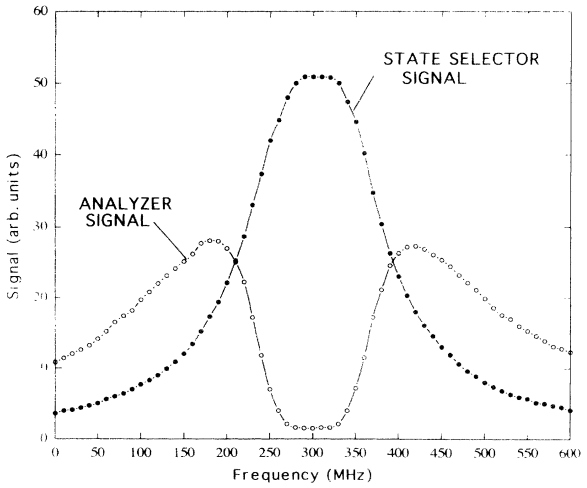

FIG. 5. Typical optical resonances observed with 535-nm fluorescence in the state selector and analyzer.

At the peak of the optical resonance the state selector fluorescent signal for the up beam is typically 6×10^9 photoelectrons (pe)/s, and the analyzer fluorescent signal at optical resonance and at the center of the $\pm\pi/4$ rf resonance is $\approx 8\times 10^7$ pe/s. These signals are so large that it is unnecessary to use all eight photomultiplier dynode states. Instead, we connect the last four dynodes to the anode, and operate each tube at moderately low voltage, where the gain is approximately 600. Each photomultiplier tube (PMT) is followed by a preamplifier with two automatically controlled gain settings (high when in analyzer mode, low when in state selector mode). The preamplifier outputs are fed to gated integrators, a 12 bit analog-to-digital converter, and a computer for data processing.

D. The electric field

The electric field plates, constructed of 6Al4V titanium alloy,[1] are 100 cm long (x) and 5 cm wide (y); the gap between the plates is 2.27 mm (z). The plates are supported in a rigid aluminum alloy structure with fused silica insulating spacers. The high voltage is supplied by two separate power supplies [Glassman: WG 30P10 (positive); 20N05 (negative)]. These are connected via standard high voltage cables to an automatically actuated double-pole–double-throw vacuum high voltage switch, followed by a current monitor, a 10^7-Ω current-limiting resistor in each line, vacuum feedthroughs, and finally the plates. The combined capacitance of the plates and of the high voltage cables feeding them is ≈ 1000 pF and the charging time constant is ≈ 0.010 s.

After the plates were machined and surface ground, they were degreased and washed in a sequence of baths: hot alkali solution, hot H_2SO_4, HNO_3-HF, and finally deionized water. After assembly in the vacuum system and evacuation, the plates must be "conditioned" in order to hold a high field without drawing excessive leakage current. The following procedure is employed and is always effective: argon gas is admitted to the vacuum system at a pressure of $\approx 10^{-3}$ torr and the polarity of the field is reversed about once every 10 or 20 s as its magnitude is gradually increased. The leakage current, usually quite high at first, subsides over a period of ≈ 24 h, and is deemed to be acceptable when it is less than or equal to 10^{-8} A for $E \approx 140$ kV/cm. The argon is then pumped out, and the plates are ready for service. Presumably the argon ions sputter away small prominences on the plates that would otherwise cause field emission.

[1] 6 Al 4V denotes 6 at. % Al, 4 at. % V.

E. The magnetic field

Magnetic field B_z is generated by two coils of length 184 cm (x), width 36 cm (y), and separation 20.5 cm (z) (see Fig. 6). The coils are placed symmetrically with respect to the beam axis in y and z coordinates, and symmetrically with respect to the midplane in x. Each coil has 70 turns, and they are connected in series. The power supply for the z coils is of critical importance because noise from magnetic field fluctuations due to variability of the current can be very significant (the rf resonance frequency is directly proportional to this current). For some time and for a wide variety of measurements, we employed a commercial constant-current power supply of high quality (Northhills TC 602). However its rms current fluctuations δI are proportional to I and become intolerable at the relatively large values of B_z that are preferred to minimize the geometric phase effect (see Sec. III B). Thus, one of us designed and constructed a constant-current power supply of much lower noise, that has proven to be very successful [24], and was employed for almost all of the EDM data reported here. A pair of coils similar to those employed for B_z is used to generate a magnetic field in the y direction. Each y coil has 18 turns, and these are connected in series and powered by a constant-current power supply. Four coils are employed to generate a magnetic field in the x direction for diagnostic purposes. Their planes are perpendicular to the beam axis (x), and they are spaced at distances of 12 and 40 cm above and below the midplane of the beam axis. The outer x coils have five turns, the inner ones four turns, and they each have an effective radius of 25 cm. These coils can be connected in series or connected independently to a power supply. The utility of the latter procedure shall be explained in Sec. III B. In addition, a set of "gradient" wires is installed to produce large magnetic field gradients [see Figs. 7(a)–7(d) and 8]. These are used in auxiliary measurements of the $\mathbf{E}\times\mathbf{v}$ effect (see Sec. III A).

The main vacuum chamber and system of magnetic coils and wires are surrounded by four large concentric cylindrical magnetic shields with four end plates on each end. These were fabricated from 0.76-mm sheet (Conetic AA Alloy, Magnetic Shield Division, Perfection Mica Co.) and carefully annealed at 1100 °C in a hydrogen atmosphere. They provide a shielding factor of better than

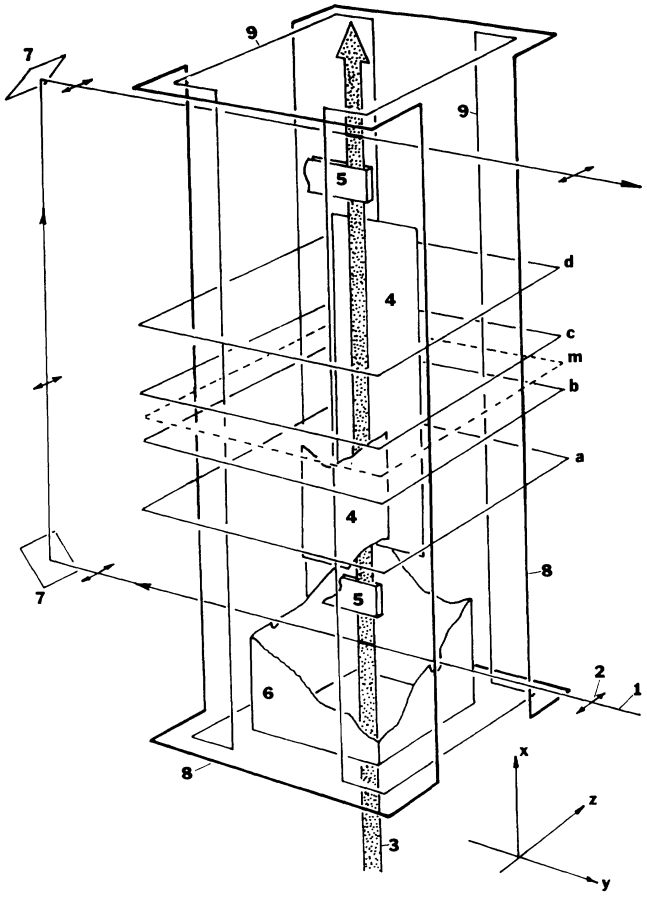

FIG. 6. Schematic perspective drawing (not to scale) indicating placement of magnetic field coils. (1) 378-nm laser beam; (2) linear polarization of laser beam; (3) up-atomic beam; (4) electric field plates; (5) RF1,2; (6) main vacuum chamber; (7) mirrors; (8) z coils; (9) y coils; (a), (b), (c), and (d) x coils 1–4, respectively; (m) medium plane. Not shown, state selector, analyzer, slits, etc.

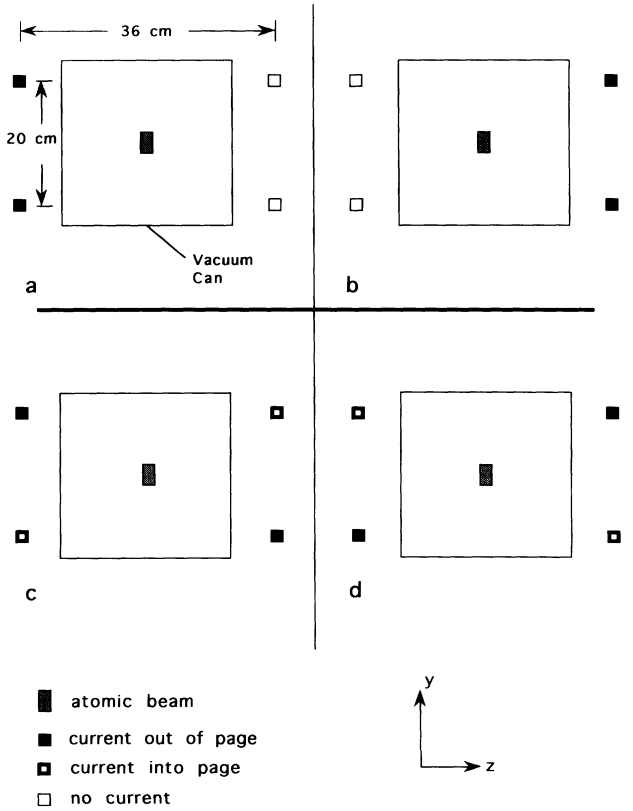

FIG. 7. (a) or (b) Two-wire arrangement (configuration 1). This produces a gradient $\partial B_z/\partial y$ at the beam axis. Wires and atomic beam are perpendicular to page. (c) or (d) four-wire arrangement (configuration 2). This produces a gradient $\partial B_z/\partial z$ at the beam axis.

10^4 for ambient magnetic fields in the y,z directions, and between 10^3 and 10^4 for fields in the x direction. The shields are equipped with a set of coils for deGaussing. For the latter purpose, we employ large currents at 60 Hz, which are gradually reduced to zero by means of a variable autotransformer. This procedure is simple but effective.

With the coils and shields in place and the latter degaussed, rf magnetic resonance measurements revealed that the average magnitude of B_z along the beam axis between RF1 and RF2 (a distance of 120 cm) was 4% larger than the value of B_z at RF1 and RF2. To compensate for this and to ensure that the Ramsey resonance center falls at the center of each broad "Rabi" resonance due to the individual rf regions, we employ a pair of small Helmholtz "trim" coils at RF1 and RF2. Each pair has 9 cm dia and ten turns per coil. They are connected in series and powered by a commercial constant-current power supply.

F. rf magnetic resonance

In Sec. II A an idealized description was given of the evolution of the $6P_{1/2}$, $F=1$ state between the state selector and analyzer. We now consider this evolution in more detail, in order to take into account the velocity distribution of the beam, the dependence of the signal on applied frequency, the quadratic Stark effect, the $\mathbf{E}\times\mathbf{v}$ effect, and the geometric phase. To begin, we recall Eq. (2), which describes the $F=0$ state immediately after optical pumping state selection.

Each oscillating rf field $B_1\cos(\omega t)\hat{\mathbf{x}}$ (in RF1) and $B_1\cos(\omega t+\alpha)\hat{\mathbf{x}}$ (in RF2) may be thought of as a superposition of two counterrotating fields of applied frequency ω in the xy plane. We ignore the "antiresonant" rotating components, and assume that $|\omega-\omega_0| \ll v/l$ where ω_0 is the resonance frequency, and l is the length of each RF region. The latter assumption means that we neglect the difference between ω and ω_0 in these regions, and consider its effect only in the relatively long region between RF1 and RF2. In other words, we confine ourselves to the central portion of the Rabi resonance curve, where the Ramsey fringes are fully developed. Then it can be shown that immediately after passage through RF1, ψ is transformed to

$$\psi' = \begin{vmatrix} \frac{-i}{\sqrt{2}}\sigma \\ \mu \\ \frac{-i}{\sqrt{2}}\sigma \end{vmatrix}, \tag{9}$$

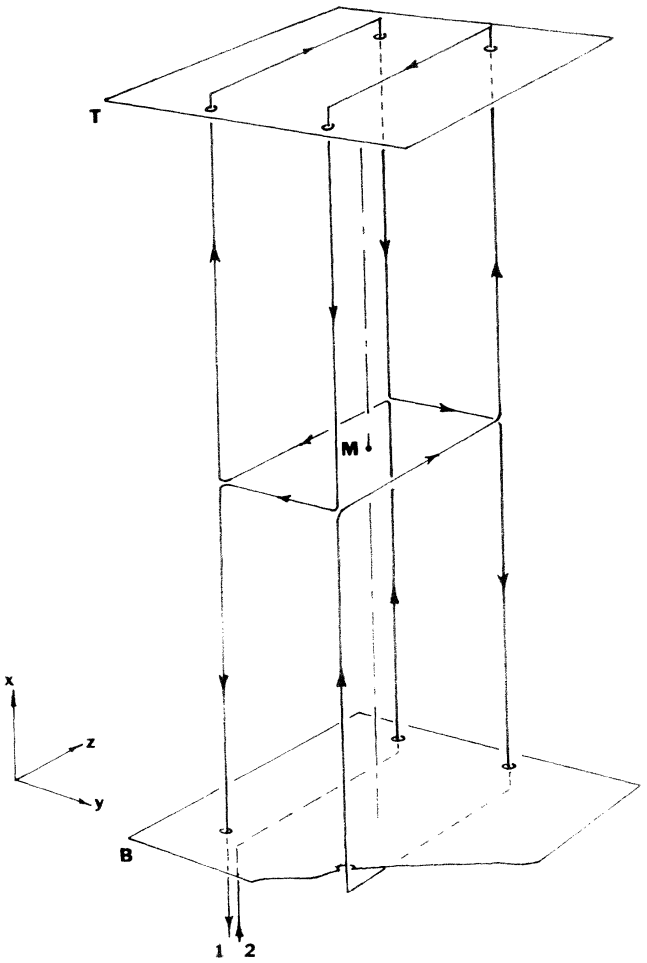

FIG. 8. Odd-x four-wire arrangement (configuration 3). This produces a gradient $\partial B_z/\partial z$ odd in x about the midpoint m, at the beam axis. 1,2 are input, output connections. B,T are innermost bottom and top horizontal magnetic shield end caps. See also Fig. 14.

where

$$\sigma = \sin\left|\gamma B_1 \frac{l}{2v}\right|, \qquad \mu = \cos\left|\gamma B_1 \frac{l}{2v}\right|, \tag{10}$$

$\gamma = 2.91\times10^6$ rad/G-s is the gyromagnetic ratio, and in (9) as previously, ψ' is expressed in the rotating frame.

The wave function evolves further in the region between RF1 and RF2. At the entrance of RF2, it can be expressed as

$$\psi' = \begin{vmatrix} \frac{-i}{\sqrt{2}}\sigma \exp\left\{i\eta_B\left[\omega T - \int_0^T \omega_0 dt\right] - i\eta_E\varepsilon - i\eta_E\varepsilon_{\text{geo}}\right\} \\ \mu e^{i\Phi} \\ \frac{-i}{\sqrt{2}}\sigma \exp\left\{-i\eta_B\left[\omega T - \int_0^T \omega_0 dt\right] + i\eta_E\varepsilon + i\eta_E\varepsilon_{\text{geo}}\right\} \end{vmatrix}, \tag{11}$$

where $T=L'/v$ is the time of transit from RF1 to RF2 with $L'=120$ cm the distance between these regions, $\eta_E\varepsilon_{\rm geo}$ is a geometric phase, and Φ is a "quadratic Stark effect" phase. (The latter quantities will be discussed below.) The resonance frequency ω_0 is proportional to the total magnetic field B' in the rest frame of the atom:

$$\omega_0=\gamma B' \ . \tag{12}$$

However,

$$\mathbf{B}'=\mathbf{B}+\frac{1}{c}\mathbf{E}\times\mathbf{v} \ , \tag{13}$$

where $\mathbf{B}$ is the applied magnetic field in the laboratory frame. Hence in (12), we have

$$B'=\left[\left[\mathbf{B}+\frac{1}{c}(\mathbf{E}\times\mathbf{v})\right]\cdot\left[\mathbf{B}+\frac{1}{c}(\mathbf{E}\times\mathbf{v})\right]\right]^{1/2} \ . \tag{14}$$

Since $|\mathbf{B}|\gg|\mathbf{E}\times\mathbf{v}|/c$, we may expand the square root in (14):

$$B'\approx|\mathbf{B}|+\frac{\mathbf{E}\times\mathbf{v}\cdot\mathbf{B}}{c|\mathbf{B}|}+\frac{(\mathbf{E}\times\mathbf{v})^2}{2c^2|\mathbf{B}|} \ . \tag{15}$$

The third term on the right-hand side of (15) is ordinarily insignificant because it is small in magnitude and is even under reversal of $\mathbf{E}$ and $\mathbf{B}$. However, the second $(\mathbf{E}\times\mathbf{v})$ term is important, since it is odd under both $\mathbf{E}$ and $\mathbf{B}$ reversal. (Detailed analysis of possible contributions of the $\mathbf{E}\times\mathbf{v}$ effect to systematic errors are given in Sec. III A.) For the present, we merely note that although $\mathbf{E}$ and $\mathbf{B}$ fields are nominally parallel, we cannot exclude the possibility of small mutually orthogonal components of these fields. Thus, the second term in (15) is generally nonzero, although it is nearly equal and opposite for the up and down beams, and

$$\omega_0=\gamma\left[|\mathbf{B}|+\frac{\mathbf{E}\times\mathbf{v}\cdot\mathbf{B}}{|\mathbf{B}|}\right]=\omega_{00}+\omega_{0,\mathbf{E}\times\mathbf{v}} \ . \tag{16}$$

It is convenient to define

$$\eta_E\varepsilon_{\mathbf{E}\times\mathbf{v}}=\int_0^T\omega_{0,\mathbf{E}\times\mathbf{v}}dt \ . \tag{17}$$

Then, making use of (16) and (17) we may rewrite (11) as follows:

$$\psi'=\begin{pmatrix} \frac{-i}{\sqrt{2}}\sigma\exp\left\{i\eta_B\left[\omega T-\int_0^T\omega_{00}dt-\eta_E\varepsilon_{\mathbf{E}\times\mathbf{v}}\right]-i\eta_E\varepsilon-i\eta_E\varepsilon_{\rm geo}\right\} \\ \mu e^{i\Phi} \\ \frac{-i}{\sqrt{2}}\sigma\exp\left\{-i\eta_B\left[\omega T-\int_0^T\omega_{00}dt-\eta_E\varepsilon_{\mathbf{E}\times\mathbf{v}}\right]+i\eta_E\varepsilon+i\eta_E\varepsilon_{\rm geo}\right\} \end{pmatrix} . \tag{18}$$

The geometric phase $\eta_E\varepsilon_{\rm geo}$ also arises from adiabatic evolution of the $6P_{1/2}$, $F=1$ state vector in the total magnetic field $\mathbf{B}'=\mathbf{B}+\mathbf{E}\times\mathbf{v}/c$. In the present experiment, $|B_z|$ is much larger than all other components of $\mathbf{B}$. It can then be shown [25] that

$$\eta_E\varepsilon_{\rm geo}\approx\int_0^T\frac{1}{B_z^2}\left[B_x\frac{\partial}{\partial t}\left[B_y+\frac{E_z v}{c}\right]-\frac{\partial B_x}{\partial t}\left[B_y+\frac{E_z v}{c}\right]\right]dt \ . \tag{19}$$

Of course in (19) we are concerned only with that part of $\varepsilon_{\rm geo}$ that changes sign with E_z. We therefore drop the terms independent of E and make the change of variables $x=vt$ in (19) to obtain

$$\eta_E\varepsilon_{\rm geo}\approx\frac{v}{c}\int_0^{L'}\frac{1}{B_z^2}\left[B_x\frac{\partial}{\partial x}(E_z)-\frac{\partial B_x}{\partial x}(E_z)\right]dx \ . \tag{20}$$

Furthermore, $\partial E_z/\partial x$ is essentially zero except in those small regions (of length several mm) at either end of the electric field plates where E turns on or off. Over these short lengths, B_z and B_x are quite constant. Taking this into account and transforming the second term on the right hand side of (20) by integration by parts, we arrive at the expression

$$\varepsilon_{\rm geo}\approx\frac{v}{c}\frac{(B_{x1}-B_{x2})|E_z|}{B_z^2} \ , \tag{21}$$

where B_{x1}, B_{x2} are the values of B_x at the entrance and exit of the electric field, respectively. The quantity $\varepsilon_{\rm geo}$ has the same sign for up and down beams, since in switching from up beam to down beam, both v and $(B_{x1}-B_{x2})$ change sign. Further discussion of the geometric phase is given in Sec. III B.

The quadratic Stark effect phase Φ arises because the $6P_{1/2}$, $F=1$, $m_F=0$ state is shifted downward with respect to the $m_F=\pm1$ components in electric field $\mathbf{E}$ by approximately $\delta\approx560\ E^2$ Hz, where E is here expressed in units of 10^5 V/cm [26]. This shift is caused in part by relatively large nS state hyperfine splittings, and in part by second-order Stark polarizability. In the presence of B_z, there is an analogous and extremely small relative shift of $m_F=\pm1$ components in addition to that caused by the usual Zeeman effect, but this shift has negligible consequences (see Sec. III C). From δ we obtain

$$\Phi=2\pi\delta\frac{L}{v}$$

or

$$\Phi\approx\frac{3.5\times10^5E^2}{v}\ \text{rad} \ , \tag{22}$$

where in (22) E is again expressed in units of 10^5 V/cm.

The wave function ψ'' of (18) evolves further as the atom passes through RF2, and it can be shown that this results in a signal in the analyzer region proportional to

$$S=\langle a-b\cos^2[u+\alpha-\eta_E(\varepsilon_{\mathbf{E}\times\mathbf{v}}+\eta_B\varepsilon_{\rm geo}+\eta_B\varepsilon)]+c\cos[u+\alpha-\eta_E(\varepsilon_{\mathbf{E}\times\mathbf{v}}+\eta_B\varepsilon_{\rm geo}+\eta_B\varepsilon)]\rangle+\beta \ . \tag{23}$$

In this formula, $\langle\cdots\rangle$ means an average over the veloci-

ty distribution [Eq. (8)], α is the relative phase of RF2 and RF1, and β is a small contribution due to background (e.g., scattered 378-nm light that reaches the phototubes). Also,

$$u=\omega T-\int_0^T \omega_{00}dt=[\omega-\langle\omega_{00}\rangle]T\ , \tag{24}$$

while

$$a=1-\mu^4,\quad b=\sigma^4,\quad c=2\mu^2\sigma^2\cos\Phi\ . \tag{25}$$

If the beams were monoenergetic we could choose B_1 so that $\gamma B_1 l/2v=\pi/2$. In this case we would have $\sigma=1$, $\mu=0$, and hence $a=b=1$, $c=0$. If in addition u, ε_{geo}, and $\varepsilon_{\text{E}\times\text{v}}$ were zero, the present formulation would reduce to the ideal case discussed in Sec. II A, and (23) would reduce to (7) for $\alpha=\pm\pi/4$.

Typical plots of the signal versus applied radio frequency (Ramsey resonance fringes), are shown in Fig. 9 for $\alpha=\pm3\pi/4$, $B_z=0.4$ G and $E=0$. These curves are in excellent agreement with numerical calculations based on (8). Experimental curves of similar quality are obtained in many measurements over the range $0.012\le B_z\le 1$ G, for $E=0$ and $E\neq0$. Above 1 G the quality of the fringes deteriorates somewhat, presumably because of excessive inhomogeneity of B_z in the individual regions RF1,2. During EDM data acquisition and for many other purposes, scans similar to Fig. 9 but with higher resolution and confined to frequencies within ±20 Hz of the resonance center are made periodically. The crossing of the curves for $\alpha=\pm3\pi/4$ at the resonance center is found by a computer algorithm and used to determine the resonance frequency, and thus to correct the frequency synthesizer. The latter instrument (Hewlett Packard 8904 A) has a two-channel output with computer controlled frequency and relative phase.

G. Analysis of signals and data acquisition

We next describe how asymmetry data are assembled and analyzed. As previously mentioned, the goal of the experiment is to determine ε by observing the change in signal S when the electric and magnetic fields are reversed. However, as is evident from (23), the signal is also a function of the parameters a, b, c, u, $\varepsilon_{\text{E}\times\text{v}}$, and ε_{geo}, and some of these quantities depend on the velocity (in different ways), and are not in general identical for the up and down beams. This rather complicated situation is dealt with effectively by observing the signal, not only when E and B are reversed, but also when other external parameters are varied. Periodic change of the rf phase reduces atomic-beam noise, and use of all four phases $\pm\pi/4$, $\pm3\pi/4$ eliminates the term proportional to c in (23), and thus the troublesome quadratic Stark shift phase Φ. Switching back and forth from up to down beam permits near elimination of the $\text{E}\times\text{v}$ effect. Finally, we periodically change the applied frequency $f=\omega/2\pi$ from 1 Hz above to 1 Hz below the resonance frequency $f_0=\langle\omega_{00}\rangle/2\pi$. The latter procedure enables us to calibrate the rate of change of the signal with respect to applied frequency on resonance (this is related to the "analyzing power" of the system, to be defined below).

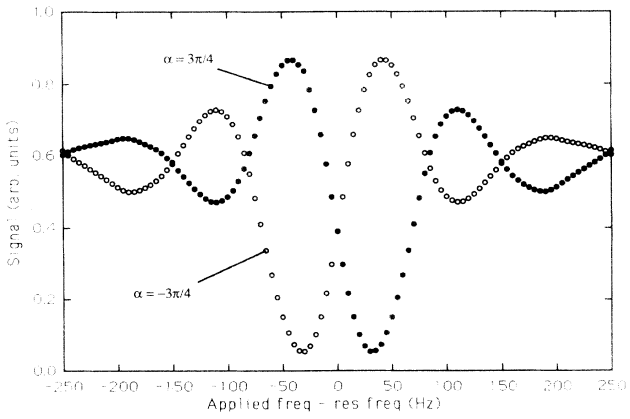

FIG. 9. Typical observed "Ramsey" fringes for $\alpha=\pm3\pi/4$.

We now describe how this program is carried out, starting from (23). Close to resonance and for $\alpha=\pm\pi/4$ or $\pm3\pi/4$, the right hand side of (23) for either beam may be expanded to first order in the small quantities u, ε, $\varepsilon_{\text{E}\times\text{v}}$, and ε_{geo}:

$$\begin{aligned}
&S(\alpha=-\pi/4)\\
&\quad=\left\langle a-\frac{b}{2}\{1+2[u-\eta_E\varepsilon_{\text{E}\times\text{v}}-\eta_E\eta_B(\varepsilon+\varepsilon_{\text{geo}})]\}\right\rangle\\
&\qquad+\left\langle\frac{c}{\sqrt{2}}\{1+[u-\eta_E\varepsilon_{\text{E}\times\text{v}}-\eta_E\eta_B(\varepsilon+\varepsilon_{\text{geo}})]\}\right\rangle+\beta\ ,\\
&S(\pi/4)\\
&\quad=\left\langle a-\frac{b}{2}\{1-2[u-\eta_E\varepsilon_{\text{E}\times\text{v}}-\eta_E\eta_B(\varepsilon+\varepsilon_{\text{geo}})]\}\right\rangle\\
&\qquad+\left\langle\frac{c}{\sqrt{2}}\{1-[u-\eta_E\varepsilon_{\text{E}\times\text{v}}-\eta_E\eta_B(\varepsilon+\varepsilon_{\text{geo}})]\}\right\rangle+\beta\ ,\\
&S\left(\frac{3\pi}{4}\right)\\
&\quad=\left\langle a-\frac{b}{2}\{1+2[u-\eta_E\varepsilon_{\text{E}\times\text{v}}-\eta_E\eta_B(\varepsilon+\varepsilon_{\text{geo}})]\}\right\rangle\\
&\qquad-\left\langle\frac{c}{\sqrt{2}}\{1+[u-\eta_E\varepsilon_{\text{E}\times\text{v}}-\eta_E\eta_B(\varepsilon+\varepsilon_{\text{geo}})]\}\right\rangle+\beta\ ,\\
&S\left(-\frac{3\pi}{4}\right)\\
&\quad=\left\langle a-\frac{b}{2}\{1-2[u-\eta_E\varepsilon_{\text{E}\times\text{v}}-\eta_E\eta_B(\varepsilon+\varepsilon_{\text{geo}})]\}\right\rangle\\
&\qquad-\left\langle\frac{c}{\sqrt{2}}\{1-[u-\eta_E\varepsilon_{\text{E}\times\text{v}}-\eta_E\eta_B(\varepsilon+\varepsilon_{\text{geo}})]\}\right\rangle+\beta\ .
\end{aligned}\tag{26}$$

We now construct the following linear combination of signals (for the up beam):

$$\begin{aligned}
K_u&=\left[\sum_{E\pm}\left[\sum_{\alpha=-\frac{\pi}{4},\frac{3\pi}{4}} S(f-f_0=+1\text{ Hz})\right.\right.\\
&\qquad\left.\left.+\sum_{\alpha=+\frac{\pi}{4},-\frac{3\pi}{4}} S(f-f_0=-1\text{ Hz})\right]\right]\\
&=\left\langle 8a-4b-8b\frac{2\pi L'}{v}\right\rangle+8\beta_U
\end{aligned}\tag{27}$$

and

$$K'_U=\left[\sum_{E\pm}\left[\sum_{\alpha=\frac{\pi}{4},\frac{3\pi}{4}} S(f-f_0=-1\text{ Hz})+\sum_{\alpha=+\frac{\pi}{4},-\frac{3\pi}{4}} S(f-f_0=+1\text{ Hz})\right]\right]$$
$$=\left\langle 8a-4b+8b\frac{2\pi L'}{v}\right\rangle+8\beta_U\ . \tag{28}$$

Note that in (27) and (28) we sum over E polarities. From (27) and (28) we form the asymmetry

$$\Delta_A^U\equiv\frac{K'_U-K_U}{K'_U+K_U}=\frac{2\pi L'\left\langle\frac{b}{v}\right\rangle}{\left\langle a-\frac{b}{2}\right\rangle+\beta_U}\ . \tag{29}$$

The analyzing power A_U for the up beam is defined as

$$A_U\equiv\frac{\Delta_A^U}{2\pi\frac{L'}{\langle v\rangle}}=\frac{\langle v\rangle_U\left\langle\left[\frac{b}{v}\right]_U\right\rangle}{\left\langle a_U-\frac{b_U}{2}\right\rangle+\beta_U}\ , \tag{30a}$$

where subscripts U for "up" are written explicitly. Similarly, for the down beam we have

$$A_D\equiv\frac{\Delta_A^D}{2\pi\frac{L'}{\langle v\rangle}}=\frac{\langle v\rangle_D\left\langle\left[\frac{b}{v}\right]_D\right\rangle}{\left\langle a_D-\frac{b_D}{2}\right\rangle+\beta_D}\ . \tag{30b}$$

For monoenergetic beams with optimum rf voltage, and when $\beta=0$, we would have $a=1$, $b=1$, and thus $A_U=A_D=2$. In fact, because of velocity distribution (8), the optimum values of $\langle a\rangle$, $\langle b\rangle$ are $\langle a\rangle\approx0.86$, $\langle b\rangle\approx0.65$, and we expect $A_{U,D}\approx1.20$. Figure 10 shows a plot of observed analyzing powers for up and down beams as a function of applied rf voltage.

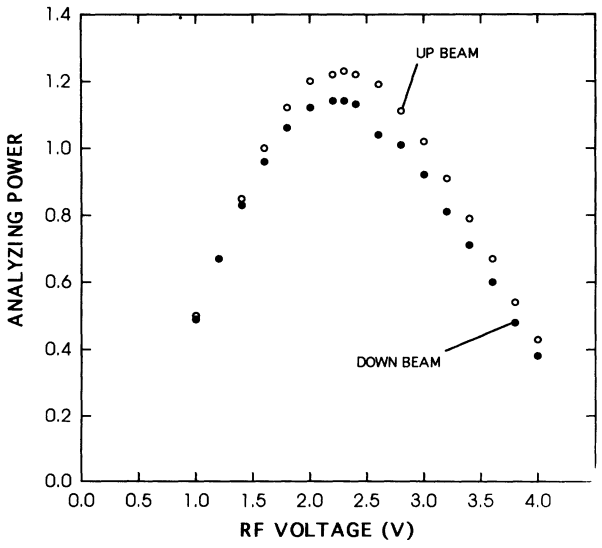

FIG. 10. Observed analyzing powers for up and down beams, as a function of rf voltage. The optimum setting of the latter is ≈2.3 V.

Now returning to (23) we consider coefficient c, which depends on the quadratic Stark phase Φ. This is checked by measuring S as a function of E for $\alpha=0$ or $\alpha=\pi$ and where $\omega=\langle\omega_{00}\rangle$. For these conditions, (23) becomes

$$S=\langle a-b\pm c\rangle+\beta\ , \tag{31}$$

where $\pm$ here refer to $\alpha=0,\pi$, respectively, and we ignore the extremely small contributions from ε, ε_{geo}, and $\varepsilon_{E\times v}$. The expected dependence of S on E is shown in Fig. 11, where the curve is calculated for $\alpha=0$, optimum rf voltage, and $\delta=560\,E^2$ Hz (E in 10^5 V/cm). Observations of S versus E for $\alpha=0$ are also shown in Fig. 11.

If the magnitude of the applied E field depends slightly on its polarity, because of some imperfection in the high voltage switches, cables, etc., then c also depends to some extent on the polarity of E. To check this we construct the following quantities for either beam:

$$C_1(\pm E)=\sum_{f-f_0=\pm1\text{ Hz}}\ \sum_{\alpha=\pm\frac{\pi}{4}} S$$
$$=\left\langle 4a-2b+\frac{4c(\pm E)}{\sqrt{2}}\right\rangle+4\beta\ ,$$
$$C_2(\pm E)=\sum_{f-f_0=\pm1\text{ Hz}}\ \sum_{\alpha=\pm\frac{3\pi}{4}} S \tag{32}$$
$$=\left\langle 4a-2b-\frac{4c(\pm E)}{\sqrt{2}}\right\rangle+4\beta\ .$$

From these we form

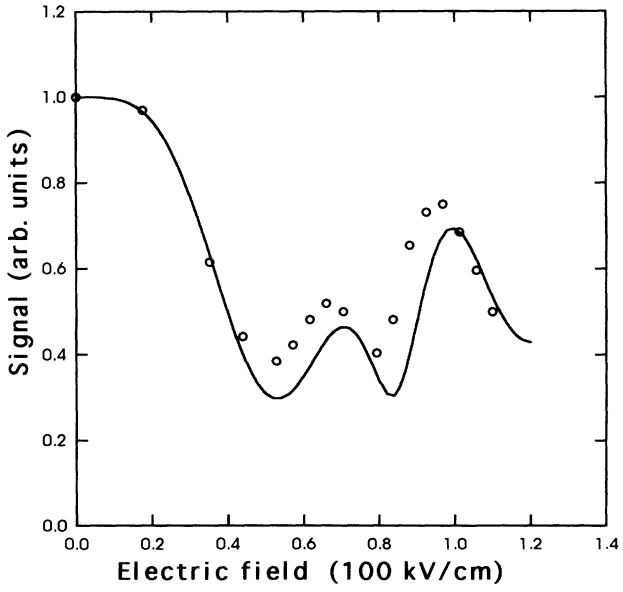

FIG. 11. Solid curve; calculated signal vs E at rf resonance for $\alpha=0$, assuming $\delta=560$ Hz and optimum rf voltage, normalized to unity at $E=0$. Discrete points; observed signal vs E at rf resonance for $\alpha=0$, normalized to unity at $E=0$. The qualitative features of the calculated curve are reproduced by the observations.

$$\Delta_C(\pm E)=\sqrt{2}A_{U,D}^{-1}\frac{C_1(\pm E)-C_2(\pm E)}{C_1(\pm E)+C_2(\pm E)}=\frac{\langle c(\pm E)\rangle}{\langle v\rangle\left\langle\frac{b}{v}\right\rangle}\ . \tag{33}$$

Then, we define

$$\begin{aligned}\delta\Delta_C&\equiv\tfrac{1}{2}[\Delta_C(+E)-\Delta_C(-E)]\ ,\\ \bar{\Delta}_C&\equiv\tfrac{1}{2}[\Delta_C(+E)+\Delta_C(-E)]\end{aligned} \tag{34}$$

for either beam. The quantity $\delta\Delta_C$ provides a sensitive measure of the variation of $|E|$ with polarity. Frequent observations of $\delta\Delta_C$ are thus useful for detecting possible malfunctions in the high voltage system. The quantity $\bar{\Delta}_C$ is the average over both E polarities of $\langle c\rangle/(\langle v\rangle\langle b/v\rangle)$. In Fig. 12, we plot $\langle c\rangle/(\langle v\rangle\langle b/v\rangle)$ versus rf voltage for $E=0$ and compare it to a calculation of the same quantity based on (8) and (25). We think that the discrepancies between calculations and observations in Figs. 11 and 12 arise from spatial inhomogeneity in the rf fields. These discrepancies are unimportant for the EDM measurement.

We now consider combinations of the signals in (26) that permit us to measure ε, $\varepsilon_{\rm geo}$, and $\varepsilon_{\mathbf{E}\times\mathbf{v}}$. Here it is important to note that ε and $\varepsilon_{\rm geo}$ are very nearly the same for the up and down beams while $\varepsilon_{\mathbf{E}\times\mathbf{v}}$ is very nearly opposite for these two beams. In what follows it will be convenient to employ the following notation to describe the signals of (26): $i=1,2,3,4$ for $\alpha=-\pi/4,\pi/4,3\pi/4,-3\pi/4$, respectively; $j=1,2$ for $f-f_0=\pm1$ Hz, respectively; $k=1,2$ for $E>0, E<0$, respectively; and $m=1,2$ for up, down beams, respectively. We then construct the following linear combinations of signals $S(i,j,k,m)$ for the up beam:

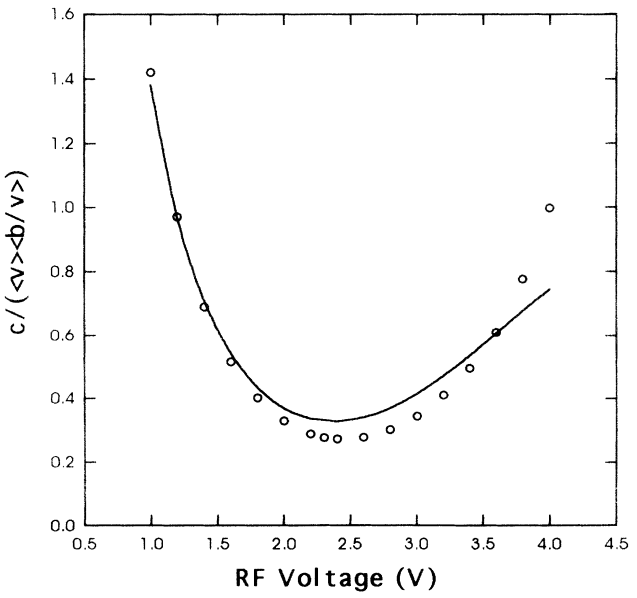

FIG. 12. Variation of $c/\langle v\rangle\langle b/v\rangle$ with rf voltage for $E=0$. Solid curve, calculation. Points, observations.

$$U_1\equiv S(1,1,1,1)+S(2,1,2,1)+S(3,1,1,1)+S(4,1,2,1)$$
$$=4\left|\left\langle a-\frac{b}{2}+b(\varepsilon_{\mathbf{E}\times\mathbf{v}}+\eta_B\varepsilon+\eta_B\varepsilon_{\rm geo})\right\rangle+\beta_U\right|\ , \tag{35}$$

$$U_2\equiv S(1,1,2,1)+S(2,1,1,1)+S(3,1,2,1)+S(4,1,1,1)$$
$$=4\left|\left\langle a-\frac{b}{2}-b(\varepsilon_{\mathbf{E}\times\mathbf{v}}+\eta_B\varepsilon+\eta_B\varepsilon_{\rm geo})\right\rangle+\beta_U\right|\ , \tag{36}$$

$$U_3\equiv S(1,2,1,1)+S(2,2,2,1)+S(3,2,1,1)+S(4,2,2,1)$$
$$=4\left|\left\langle a-\frac{b}{2}+b(\varepsilon_{\mathbf{E}\times\mathbf{v}}+\eta_B\varepsilon+\eta_B\varepsilon_{\rm geo})\right\rangle+\beta_U\right|\ , \tag{37}$$

and

$$U_4\equiv S(1,2,2,1)+S(2,2,1,1)+S(3,2,2,1)+S(4,2,1,1)$$
$$=4\left|\left\langle a-\frac{b}{2}-b(\varepsilon_{\mathbf{E}\times\mathbf{v}}+\eta_B\varepsilon+\eta_B\varepsilon_{\rm geo})\right\rangle+\beta_U\right|\ . \tag{38}$$

From these quantities, we form

$$\Delta_U=\frac{1}{2}\left|\frac{U_1-U_2}{U_1+U_2}+\frac{U_3-U_4}{U_3+U_4}\right|\ ,$$

which is

$$\Delta_U=\frac{\langle b_U[\varepsilon^U_{\mathbf{E}\times\mathbf{v}}+\eta_B(\varepsilon+\varepsilon_{\rm geo})]\rangle}{\left\langle a_U-\frac{b_U}{2}\right\rangle+\beta_U}\ . \tag{39}$$

In (39), we employ the symbol "U" explicitly for the up beam to indicate that the quantities so labeled may be different from the down beam. A similar expression can be constructed for the down beam:

$$\Delta_D=\frac{\langle b_D[\varepsilon^D_{\mathbf{E}\times\mathbf{v}}+\eta_B(\varepsilon+\varepsilon_{\rm geo})]\rangle}{\left\langle a_D-\frac{b_D}{2}\right\rangle+\beta_D}\ . \tag{40}$$

Now recalling expressions (31a) and (31b) for the analyzing powers $A_{U,D}$ we write

$$\Delta^+\equiv\tfrac{1}{2}\left|\frac{\Delta_U}{A_U}+\frac{\Delta_D}{A_D}\right|\approx\tfrac{1}{2}[(\varepsilon^U_{\mathbf{E}\times\mathbf{v}}+\varepsilon^D_{\mathbf{E}\times\mathbf{v}})+2\eta_B(\varepsilon+\varepsilon_{\rm geo})] \tag{41}$$

and

$$\Delta^-\equiv\tfrac{1}{2}\left|\frac{\Delta_U}{A_U}-\frac{\Delta_D}{A_D}\right|\approx\tfrac{1}{2}[\varepsilon^U_{\mathbf{E}\times\mathbf{v}}-\varepsilon^D_{\mathbf{E}\times\mathbf{v}}]\ . \tag{42}$$

In the limit of perfect spatial overlap of the up and down beams, and when both beams have the same velocity distribution, we have $\varepsilon^U_{\mathbf{E}\times\mathbf{v}}=-\varepsilon^D_{\mathbf{E}\times\mathbf{v}}$. In this case,

$$\Delta^+=\eta_B[\varepsilon+\varepsilon_{\rm geo}]\ . \tag{43}$$

Asymmetry Δ^+ is the most important observable in the experiment. From it we determine $\varepsilon+\varepsilon_{\rm geo}$; by eliminat-

ing the geometric phase contribution ε_{geo}, we obtain ε. Asymmetry Δ^- also plays a very important role, as we shall see in Sec. III A.

We next describe how the data are acquired. The gated integrator integration time is 1 ms. The system cycles through the various parameters as follows.

(a) RF—The phase of RF2 (that rf region closest to the analyzer for the up or down beam) is changed relative to that of RF1. The phase α cycles through its four values, with 50-ms data acquisition at each value, and 5-ms delay between values (to allow the atoms to move from RF2 through the analyzer region). Neglecting this delay, a full rf cycle is 200 ms.

(b) Frequency change—for most of our EDM data, $f-f_0$ was kept at one value for two full rf cycles, then reversed, with a 20-ms delay. For some of the data, $f-f_0$ was kept at one value for 16 full rf cycles, then reversed.

(c) E reversal—E is maintained at one polarity for four rf cycles, then reversed, after which we employ a 400-ms delay before resuming data collection. This delay was chosen to allow the plates to come to full charge (recall that the charging time constant is ≈ 10 ms).

(d) Beam reversal—one beam is employed for 32 full rf cycles, after which we change the beam, impose a 4-s delay, and then resume data collection. When a beam reversal occurs, the state selector becomes the analyzer and vice versa. The flux of thallium atoms into the state selector region is very large, and in the ideal case, those atoms that do not clear the slits 1,2 (or 3,4) stick to the surrounding parts. However, we have some evidence that the sticking is less than perfect, because the analyzer signal contains a very small and slowly decaying background from these atoms. The 4-s delay was chosen to reduce this effect, which was a minor annoyance but did not lead to systematic error in the EDM measurement.

A full beam period is called a "sweep," 8 sweeps constitute a "point" and 16 "points" form a "set". (Our final data, summarized in Table III, are expressed in points.) The order of the various reversals described above is systematically permuted as we proceed through the various sweeps and points to complete a set. A point takes about 5 min of real time. After it is completed, the data associated with it (including Δ^+, Δ^-, the analyzing powers $A_{U,D}$, and $\bar{\Delta}_C$ and $\delta\Delta_C$) are displayed on the computer screen, there is a brief pause in acquisition while the laser is stabilized, and the next point proceeds. After eight points the rf is stabilized as well. Ordinarily, after a set is completed, the data are printed out, and some external conditions (such as the sign of B or the parity of the high voltage cables from switch to vacuum chamber) may be changed.

TABLE III. Summary of final EDM data: d_a in units of 10^{-24} e cm. Uncertainties are statistical, 68% confidence.

194.2 kHz

	N=no. of points	Result	Result (sign correction)[a]
(a)	387	$d_a[B+E+]=4.15\pm1.35$	$d_a[B+E+]=4.15\pm1.35$
(b)	397	$d_a[B+E-]=0.70\pm1.40$	$d_a[(B+E-)]=-0.70\pm1.40$
(c)	400	$d_a[B-E+]=3.6\pm1.35$	$d_a[(B-E+)]=-3.6\pm1.35$
(d)	408	$d_a[B-E-]=-3.97\pm1.4$	$d_a[B-E-]=-3.97\pm1.4$

$$d_a[B+]=\frac{d_a[B+E+]+d_a[(B+E-)]}{2}=1.76\pm0.99$$

$$d_a[B-]=\frac{d_a[B-E-]+d_a[(B-E+)]}{2}=-3.80\pm0.99$$

$$d_a[B_{\text{even}}E_{\text{odd}}]=\frac{d_a[B+E+]-d_a[B+E-]+d_a[B-E+]-d_a[B-E-]}{4}=2.75\pm0.70$$

Final result: $d_a=\frac{d_a[B+]+d_a[B-]}{2}=-1.05\pm0.70$

35.9 kHz

	N=no. of points	Result	Result (sign correction)[a]
(a)	60	$d_a[B+E+]=12.2\pm4.1$	$d_a[B+E+]=12.2\pm4.1$
(b)	63	$d_a[B-E+]=14.5\pm4.1$	$d_a[(B-E+)]=-14.5\pm4.1$

$$\frac{d_a[B+E+]+d_a[B-E+]}{2}=13.3\pm2.8$$

$$d_a=\frac{d_a[B+E+]+d_a[(B-E+)]}{2}=-1.2\pm2.8$$

[a]See Sec. IV for a discussion of the "sign correction."

III. SYSTEMATIC EFFECTS

A. The E×v effect

We have noted previously that

$$\eta_E \varepsilon_{\mathbf{E}\times\mathbf{v}} = \int_0^T \omega_{0,\mathbf{E}\times\mathbf{v}} dt = \gamma \int_0^T \frac{\mathbf{E}\times\mathbf{v}\cdot\mathbf{B}}{c|\mathbf{B}|} dt \tag{44}$$

and that while **E** and **B** fields are nominally in the z direction, we cannot exclude the possibility of small x and y components of these fields. Furthermore, while **v** is nominally along x, it could also have small y and z components. Thus, we have

$$\frac{\mathbf{E}\times\mathbf{v}\cdot\mathbf{B}}{c|\mathbf{B}|} \approx \frac{1}{c|B_z|}[(B_y E_z - B_z E_y)v_x + (B_z E_x - B_x E_z)v_y + (B_x E_y - B_y E_x)v_z] . \tag{45}$$

In (45), the three successive terms in the square brackets are first, second, and third-order small, respectively. It can be shown that the third-order quantities are negligible. Hence (45) can be written

$$\frac{\mathbf{E}\times\mathbf{v}\cdot\mathbf{B}}{c|\mathbf{B}|} \approx \frac{1}{c|B_z|}[(B_z E_z - B_z E_y)v_x + (B_z Ex - B_x E_z)v_y] . \tag{46}$$

Now, the observable Δ^+ from which the EDM is determined [Eq. (41)] contains the term

$$(\varepsilon^U_{\mathbf{E}\times\mathbf{v}} + \varepsilon^D_{\mathbf{E}\times\mathbf{v}}) . \tag{47}$$

The up and down beams are arranged to have nearly equal and opposite velocities, and to overlap nearly perfectly because they pass through the same collimating slits. Nevertheless, there are residual imperfections, and we cannot expect $\varepsilon_{\mathbf{E}\times\mathbf{v}}$ to be exactly equal and opposite for the up and down beams. Thus, we must analyze the residual contributions. For this purpose, we define the z axis to be parallel to the average value of **E** for the up beam and also define the following symbols:

Velocity: up beam, v_x, v_y, v_z; and down beam, $-v_x+\delta v_x$, $-v_y+\delta v_y$, $-v_z+\delta v_z$.

Magnetic field: up beam, B_x, B_y, B_z; and down beam, $B_x+\delta B_x$, $B_y \delta B_y$, $B_z+\delta B_z$.

Electric field: up beam, E_z; and down beam, δE_x, δE_y, $E_z+\delta E_z$.

Then, forming the sum of the right-hand side of (46) for the up and down beams, expanding the resulting expression in terms of the symbols just defined, and discarding negligible terms, we arrive at the following formula:

$$\eta_E[\varepsilon^U_{\mathbf{E}\times\mathbf{v}} + \varepsilon^D_{\mathbf{E}\times\mathbf{v}}] \approx \gamma \int_0^T \left[\frac{B_y \delta v_x}{v_x} - \frac{B_x \delta v_y}{v_x} - \delta B_y + \frac{\delta E_y B_z}{E_z} \right] \frac{E_z v_x}{c|B_z|} dt . \tag{48}$$

We shall now show how various auxiliary measurements place limits on the four terms of (48). For convenience, the limits will be expressed directly in terms of an equivalent atomic EDM d_a.

1. First term

$$\gamma \int_0^T \left| \frac{B_y \delta v_x}{v_x} \right| \frac{E_z v_x}{c|B_z|} dt = \gamma \int_0^L \left| \frac{B_y \delta v_x}{v_x} \right| \frac{E_z}{c|B_z|} dx \tag{49}$$

is proportional to $\delta v_x / v_x$, and the coefficient of proportionality is

$$\gamma \int_0^T \frac{B_y E_z v_x}{c|B_z|} dt \approx \tfrac{1}{2}(\varepsilon^U_{\mathbf{E}\times\mathbf{v}} - \varepsilon^D_{\mathbf{E}\times\mathbf{v}})\eta_E = \eta_E \Delta^- . \tag{50}$$

We measure Δ^- during acquisition of EDM data, and maintain $|B_y/B_z| \le 5\times10^{-7}$ on the average by adjusting the current in the y coils to cancel B_y. We also compare the widths of the Ramsey resonances for the up and down beams, and adjust oven temperatures to ensure that $|\delta v_x / v_x| \le 0.01$. We have also investigated the dependence of Δ^+ on $\delta v_x / v_x$ when Δ^- is deliberately held at large values. From the results of these measurements, we conclude that the term (49) contributes a false d_a no larger than 5.8×10^{-26} e cm:

$$|d_a(\delta v_x)| \le 5.8\times10^{-26}\ e\ \text{cm} . \tag{51}$$

2. Second term

The second term of (48) involves the quantities $(B_x/|B_z|)\delta v_y / v_x$. The troublesome portion of B_x is that part which arises from misalignment of the z, y, and/or trim coils, and reverses when the currents to those coils are changed. We obtain the limit $|B_x/B_z| \le 0.0003$ by taking Δ^+ asymmetry data when δv_y is deliberately made very large with the aid of the half slits 1,4 (See Fig. 4): $|\delta v_y / v_x| = 2\times10^{-3}$. To determine δv_y with the slits in normal alignment, we deliberately impose a magnetic field B_x with the x coils (see Fig. 6) that is a factor of 200 larger than the limit on B_x just described, measure Δ^+, and adjust the oven y positions as necessary to minimize the portion of Δ^+ odd in applied B_x, to a level of $d_a \approx 5.8\times10^{-24}$ e cm. The result is that in normal alignment, $|\delta v_y / v_x| \le 2\times10^{-5}$. The foregoing combination of measurements results in the following limit:

$$|d_a(B_x \delta v_y)| \le 1.75\times10^{-25}\ e\ \text{cm} . \tag{52}$$

3. Third and fourth terms

The third and fourth terms in (48) are proportional to

$$\langle E_z \delta B_y - B_z \delta E_y \rangle \approx E_z \langle \delta B_y \rangle - B_z \langle \delta E_y \rangle ,$$

where $\langle \cdots \rangle$ means an average over the length L. We may write

$$\langle \delta B_y \rangle = \left\langle \frac{\partial B_y}{\partial y} \Delta y \right\rangle + \left\langle \frac{\partial B_y}{\partial z} \Delta z \right\rangle \tag{53a}$$

and

$$\langle \delta E_y \rangle = \left\langle \frac{\partial E_y}{\partial y} \Delta y \right\rangle + \left\langle \frac{\partial E_y}{\partial z} \Delta z \right\rangle , \tag{53b}$$

where Δy, Δz are the separations between the down and

up beams in y,z, respectively. However, since $\nabla\times\mathbf{B}=\nabla\times\mathbf{E}=0$ we have $\partial B_y/\partial z=\partial B_z/\partial y$, and $\partial E_y/\partial z=\partial E_z/\partial y$. Furthermore, since $\nabla\cdot\mathbf{B}=0$, $\nabla\cdot\mathbf{E}=0$ and it an be shown that $\partial B_x/\partial x$ and $\partial E_x/\partial x$ are negligibly small, we have $\partial B_y/\partial y\approx-\partial B_z/\partial z$, $\partial E_y/\partial y\approx-\partial E_z/\partial z$. It may also be shown that for our electric field plates, $\partial E_z/\partial z$ is negligible; however, this is *not* the case for $\partial E_z/\partial y$, because of possible "wedging" of the plates. This is illustrated in Fig. 13, which shows the plate surfaces in cross section (beam axis perpendicular to the page). If the plates are wedged as shown, then

$$\frac{\partial E_z}{\partial y}\approx\frac{\Delta d}{hd}E_z\ , \tag{54}$$

where $h=5$ cm is the width of the plates, $d=2.27$ mm is their separation, and Δd is the increment in separation. Taking all of this into account, we may rewrite (53a) and (53b) as follows:

$$\langle\delta B_y\rangle\approx\left\langle-\frac{\partial B_z}{\partial z}\Delta y\right\rangle+\left\langle\frac{\partial B_z}{\partial y}\Delta z\right\rangle \tag{54a}$$

and

$$\langle\delta E_y\rangle\approx\left\langle\frac{\partial E_z}{\partial y}\Delta z\right\rangle\ . \tag{54b}$$

In principle, the quantities $\partial B_z/\partial z$, $\partial B_z/\partial y$, $\partial E_z/\partial y$, Δy, and Δz may each depend on x. We thus expand them in powers of x, measured from the midpoint:

$$\frac{\partial B_z}{\partial z}=b_{z0}+b_{z1}x+b_{z2}x^2+\cdots\ , \tag{55}$$

$$\frac{\partial B_z}{\partial y}=b_{y0}+b_{y1}x+b_{y2}x^2+\cdots\ , \tag{56}$$

$$\frac{\partial E_z}{\partial y}=e_{y0}+e_{y1}+x+e_{y2}x^2+\cdots\ , \tag{57}$$

$$\Delta y=d_{y0}+d_{y1}x\ , \tag{58}$$

and

$$\Delta z=d_{z0}+d_{z1}x\ . \tag{59}$$

In (58) and (59), the expansions terminate as shown because the beam trajectories are straight, the effects of curvature due to gravitational acceleration being negligible. In fact, coefficient d_{y1} is itself negligible, because of the limits on Δv_y already established in Sec. III A 1, and it may be shown that coefficients b_{z2} and b_{y2} are also negligible. Taking all this into account, we now describe how auxiliary measurements place limits on the various terms in (54a) and (54b).

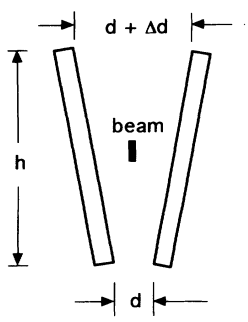

FIG. 13. Schematic diagram illustrating wedging of the electric field plates (not to scale). The actual values of Δd are ≤ 0.002 cm. Atomic beam perpendicular to page.

a. $\langle(\partial B_z/\partial z)\Delta y\rangle$. From (55) and (58) we have

$$\left\langle\frac{\partial B_z}{\partial z}\Delta y\right\rangle\approx d_{y0}b_{z0}\ . \tag{60}$$

By means of slits 1–4 we deliberately impose a large and known separation δz between the up and down beams in the z direction, and measure the resonance frequency difference between up and down beams. This is given by the formula

$$\frac{\Delta\nu}{\nu}=\frac{\delta B_z}{B_z}=\frac{1}{B_z}\left\langle\frac{\partial B_z}{\partial z}\right\rangle\delta z=\frac{1}{B_z}b_{z0}\delta z\ , \tag{61}$$

from which b_{z0} may be extracted, since all other quantities in (61) are known. At $B_z=0.4$ G, we obtain

$$|b_{z0}|\leq 8\times10^{-6}\ \text{G/cm}\ . \tag{62}$$

There are two independent methods to obtain d_{y0} in (60). In the first, we deliberately produce a large gradient $\partial B_y/\partial z=\partial B_z/\partial y=\pm3.8\times10^{-4}$ G/cm by passing a current of 1 A through the "gradient" wires in configuration 1, [Figs. 7(a) or 7(b)]. The frequency difference between up-beam and down-beam resonances is measured as in the previous paragraph, and the oven y positions are adjusted as necessary to minimize the difference. (In fact this procedure, and the procedure to minimize Δv_y are done iteratively.) In practice, this results in an average separation between the beams of $d_{y0}\leq0.0006$ cm. In the second method, we produce a gradient $\partial B_y/\partial y=\pm1.3\times10^{-3}$ G/cm by passing 1 A through the gradient wires in configuration 2 [Fig. 7(c) or 7(d)] and measure the EDM-like asymmetry Δ^+. Both these methods yield consistent results and provide a limit on the false EDM due to $\langle\Delta y\partial B_z/\partial z\rangle$:

$$|d_a(\Delta y)|\leq5.8\times10^{-26}e\ \text{cm}\ . \tag{63}$$

b. $E_z\langle(\partial B_z/\partial y)\Delta z\rangle-B_z\langle(\partial E_z/\partial y)\Delta z\rangle$. From (56), (57), and (59) we obtain

$$\begin{aligned}E_z\left\langle\frac{\partial B_z}{\partial y}\Delta z\right\rangle-B_z\left\langle\frac{\partial E_z}{\partial y}\Delta z\right\rangle&=d_{z0}\left[b_{y0}E_z-\left[e_{y0}+\frac{e_{y2}L^2}{12}\right]B_z\right]\\&+d_{z1}\left[(b_{y1}E_z-e_{y1}B_z)\frac{L^2}{12}\right]=d_{z0}A_0+d_{z1}A_1\ .\end{aligned} \tag{64}$$

and where A_0, A_1 are defined by the quantities in square brackets. Coefficients d_{z0} and d_{z1} are determined by an iterative procedure that makes use of (a) 1 A in the gradient wires in configuration 2, Figs. 7(c) or 7(d) to produce a known gradient $\partial B_z/\partial z$ that is an even function of x [see Eq. (64)] and (b) 2 A in the gradient wires of

configuration 3, Fig. 8 to produce a known gradient $\partial B_z/\partial z$ that is an odd function of x (see Fig. 14). With slits 1–4 set normally, the resonant frequency difference between the up and down beams is measured, and the oven z positions are adjusted to minimize d_{z0} and d_{z1}. In practice, one can maintain $d_{z0} \leq 0.0002$ cm and $d_{z1}L/2 \leq 0.000\,14$ cm by this extremely sensitive method. Note that the limits on d_{z0}, d_{z1}, and d_{y0} correspond to maintaining the positional stability of the oven slits to about 0.003 and 0.010 cm in the z and y dimensions, respectively. Limits on the quantities A_0 and A_1 in (66) are obtained by deliberately displacing the ovens in z to produce large and known values of d_{z0} (90 times the limit on d_{z0} in normal operation) or d_{z1} (35 times the limit on d_{z1} in normal operation) and measuring the EDM-like asymmetry Δ^+. As an additional check, the upper limit $|b_{y0}| \leq 8\times10^{-6}$ G/cm is found at $B_z = 0.4$ G, by a procedure similar to that described above for b_{z0}. We thus obtain the limits

$$|d_a(\Delta z, x \text{ even})| \leq 2.3\times10^{-25}\ e\ \text{cm}\ , \tag{65}$$

$$|d_a(\Delta z, x \text{ odd})| \leq 2.9\times10^{-25}\ e\ \text{cm}\ . \tag{66}$$

Finally, we note that the x-odd wedging effect of the E plates coupled to a nonzero value of d_{z1} caused prolonged difficulty before it was understood and eliminated.

Combining the limits of (51), (52), (63), (65), and (66) in quadrature we arrive at the total contribution from the $\mathbf{E}\times\mathbf{v}$ effect:

$$|d_a(\mathbf{E}\times\mathbf{v})| \leq 4.1\times10^{-25}\ e\ \text{cm}\ . \tag{67}$$

B. The geometric phase effect

It was earlier shown that

$$\eta_B \varepsilon_{\text{geo}} \approx \frac{v}{c}\frac{\eta_B (B_{x1}-B_{x2})|E_z|}{B_z^2}\ , \tag{68}$$

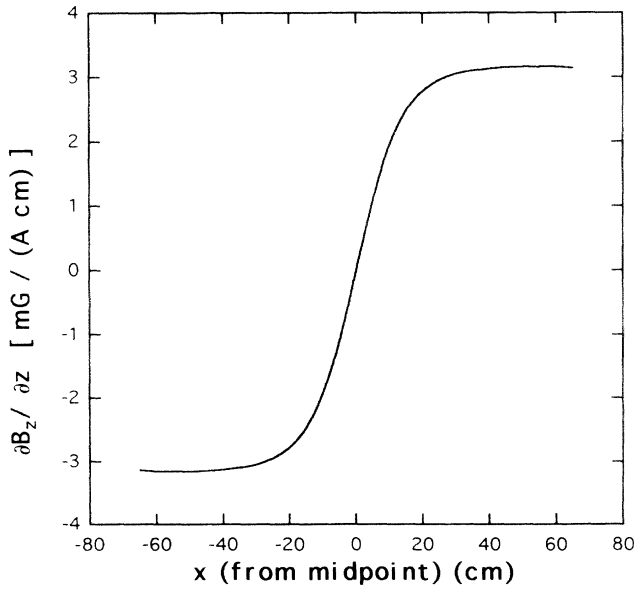

FIG. 14. Calculated values of $\partial B_z/\partial z$ vs x when 1 A is applied to the four-wire arrangement of Fig. 8.

where B_{x1}, B_{x2} are the values of B_x at the entrance and exit of the electric field, respectively. The validity of (68) is demonstrated by applying a known B_x field that takes opposite values at the two ends of the **E** field. This is done with opposite currents in the x coils 1,4 (see Fig. 6). In Fig. 15, we plot the observed values of ε_{geo} vs $Q \equiv [(B_{x1}-B_{x2})(v/c)E_z]/B_z^2$ for various values of B_z, and where $B_{x1} = -B_{x2} = 0.094$ G at $I_x = 1$ ampere, $E_z = 107$ kV/cm, and we assume that $v \approx 3.9\times10^4$ cm/s. The agreement between observed and calculated values is very satisfactory.

While strenuous efforts have been made to avoid *stray* B_x field in the apparatus, they must exist at some level, and may take different values at the entrance and exit of the **E** field. Thus, the geometric phase effect can cause a systematic error in determination of d_e. The part of $B_{x1}-B_{x2}$ that is caused by the z and trim coils reverses when the z current is reversed, and generates a contribution to $\eta_B\varepsilon_{\text{geo}}$ that is *even* under B_z reversal, and varies as $1/B_z$. In fact we have evidence for such an effect in our EDM data (see Sec. IV). Stray B_x fields from external sources that do not reverse with B_z generate a contribution to $\eta_B\varepsilon_{\text{geo}}$ that is *odd* under reversal of B_z, but varies as $1/B_z^2$. By measuring Δ^+ at low values of B_z (0.076 G, $\omega_0/2\pi = 35.9$ kHz), and extrapolating to the frequency $\omega_0/2\pi = 194.2$ kHz where the bulk of EDM data were taken, we obtain the following limit:

$$|d_a(\text{geo phase})| \leq 2.9\times10^{-25}\ e\ \text{cm}\ . \tag{69}$$

C. Miscellaneous systematic effects

Charging and leakage currents associated with the electric field plates can cause magnetic fields that change

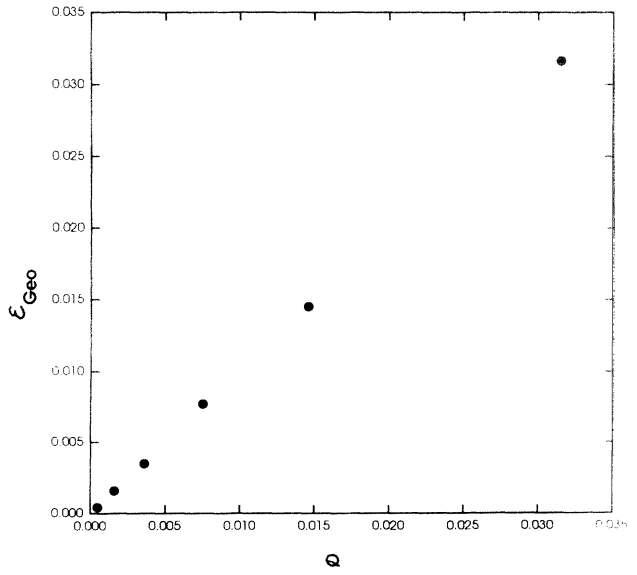

FIG. 15. Observed values of ε_{geo} plotted vs $Q = [(B_{x1}-B_{x2})vE_z]/B_z^2$ for various values of B_z, when known $B_{x1} = -B_{x2}$ is applied. The agreement between calculation and observations is excellent.

when the E polarity is reversed. The effect of charging currents is minimized by imposing a delay of 400 ms [$\approx 40\times$(charging time constant)] after each E polarity reversal, before resumption of data acquisition. When this delay is reduced to 100 ms, no change is noticed in Δ^+ at a level of 5.8×10^{-24} e cm precision in d_a. Leakage currents are maintained at a very low level (see Sec. II D). Conservative worst-case estimates of these effects yield the limit

$$|d_a(\text{leakage, charging})| \leq 1.2\times10^{-25}\ e\ \text{cm} . \quad (70)$$

We have considered other miscellaneous effects, including those due to gravitational acceleration of the beams, magnetic fields from the high voltage switch, recoil of the atoms in the state selector region due to photon absorption in optical pumping, and the following effects, each coupled to a dependence of $|E|$ on polarity through imperfections in the high voltage system: RF phase errors, the third ("E^2v^2/c^2") term in (15), and a quadratic Stark effect-induced Zeeman frequency shift between $F=1$, $m_F=\pm1$ levels. All these contributions are estimated to be less than 5×10^{-26} e cm in d_a, and hence are quite negligible in comparison to other effects already discussed.

D. Combined systematic uncertainty

We combine in quadrature the limits given in (67), (69), and (70) to obtain

$$|d_a(\text{systematic})| \leq 5.9\times10^{-25}\ e\ \text{cm} . \quad (71)$$

IV. RESULTS AND CONCLUSIONS

Table III summarizes our final EDM data. Part of the data were obtained at 35.9 kHz ($|B_z|=0.078$ G), and a much larger portion at 194.2 kHz ($|B_z|=0.42$ G). In each case data were acquired for both signs of B_z. (Some data were also acquired at very low frequencies, but these showed evidence for a breakdown of the adiabatic approximation in the geometric phase effect and in $\delta\Delta_C$. Since this is a complicated situation and not fully understood, we did not use these data.) Roughly equal amounts of 194.2-kHz data were taken for the high voltage cables "normal" and "reversed". This was done to guard against a possible systematic effect arising from the high voltage switch. Data sets with $B_z>0$ or $B_z<0$ and the cables normal or reversed are labeled $d_a[B+E+]$, $d_a[B+E-]$, $d_a[B-E+]$, or $d_a[B-E-]$. In order to compare these sets with one another, we assign an "instrumental parity" to each set: $+1$ for sets $B+E+$ and $B-E-$; -1 for sets $B+E-$ and $B-E+$. In Fig. 16, which summarizes the results at 194.2 kHz, the results for sets $B+E-$ and $B-E+$ have been multiplied by (-1); these sign-corrected data are denoted by the symbols $d_a[(B+E-)]$ and $d_a[(B-E+)]$. Figure 17 shows the distribution of points for each of the sets $B+E+$, $B+E-$, $B-E+$, $B-E-$ at 194.2 kHz. The standard deviation of each point (which requires about 5 min of real time to acquire) is about 30×10^{-24} e cm in d_a. Altogether, there are 1592 points.

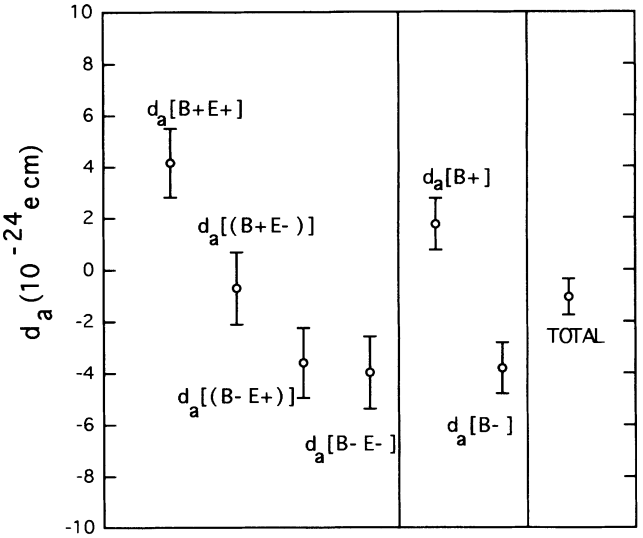

FIG. 16. Graphical summary of final 194.2-kHz data (see Table III). Error bars are 1σ. Values for $B+E-$, $B-E+$ are sign corrected and indicated by the symbols $(B+E-)$, $(B-E+)$. The point labeled $B+$ is the average of $B+E+$ and $(B+E-)$; that labeled $B-$ is the average of $(B-E+)$ and $B-E-$. The values $B+$ and $B-$ are significantly different; this indicates an asymmetry even under B reversal, consistent with a geometric phase effect due to z and/or trim coils. The point labeled *total* is the average of $B+$ and $B-$.

The results reveal a significant asymmetry that is even under B_z reversal and is consistent with the dependence $1/B_z$, hence consistent with a geometric phase effect originating from the z (and/or trim) coils themselves. There is no significant effect from electric field cable reversal, and no significant EDM effect. Combining all sets at 194.2 kHz together with appropriate signs, we obtain the final result

$$d_a=[-1.05\pm0.70\pm0.59]\times10^{-24}\ e\ \text{cm} , \quad (72)$$

where the first uncertainty in (72) is statistical and the second is systematic (71). Assuming the enhancement factor $R=-585$, we obtain the result

$$d_e=[1.8\pm1.2\pm1.0]\times10^{-27}\ e\ \text{cm} . \quad (73)$$

This yields the following upper limit on d_e:

$$|d_e| \leq 4\times10^{-27}\ e\ \text{cm} . \quad (74)$$

As stated earlier, a nonzero d_a can, in principle, arise not only from an electron EDM, but also from a nucleon EDM, a P,T-odd nucleon-nucleon interaction, and/or a P,T-odd electron-nucleon interaction. However, it can be shown [19] that d_a ($6\,^2P_{1/2}$, Tl) is very insensitive to the first two latter possibilities; these cases are more effectively investigated by other types of experiments [7–10]. On the other hand, result (72) may be used to place an upper limit on the scalar-pseudoscalar coupling constant of a P,T-odd electron nucleon interaction

$$|C_S| \leq 4\times10^{-7} . \quad (75)$$

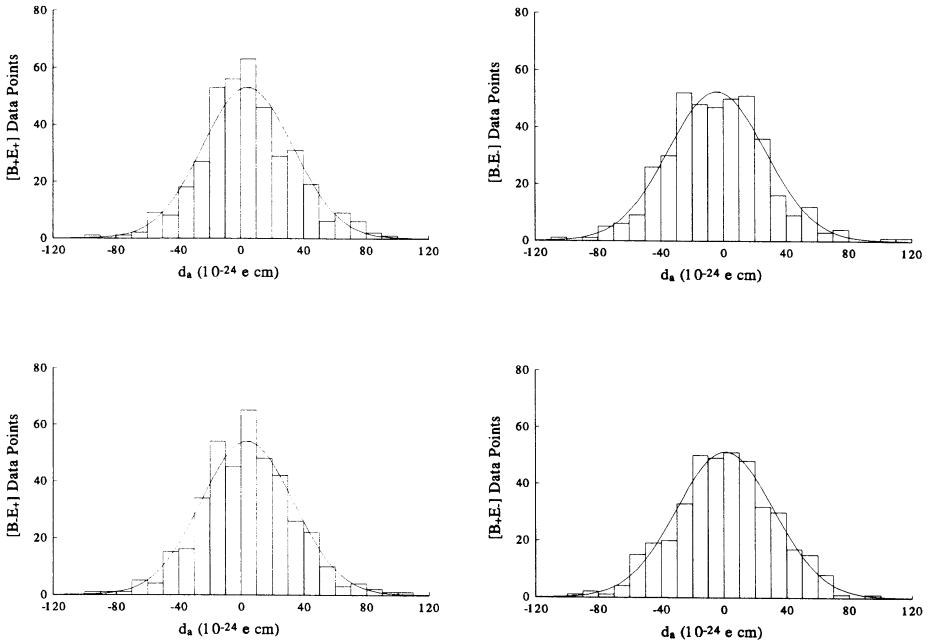

FIG. 17. Histograms of 194.2-kHz $B+E+$, $B+E-$, $B-E+$, $B-E-$ data, showing distributions of individual data points expressed in terms of d_a. In each case, the smooth curves are best-fit Gaussians.

Furthermore, Conti and Khriplovich [20] have shown that one may employ experimental limits on the electron EDM in conjunction with one-loop radiative corrections due to the P-odd part of the electroweak interaction, to obtain useful limits on possible P-even, T-odd e-e and e-N interactions. In the notation of Conti and Khriplovich, the new limits from (72) are [31]

$$\beta_e < 3\times10^{-8},\quad \beta_{eq} < 1.0\times10^{-8},\quad q_{eq} < 3\times10^{-6}\ . \tag{76}$$

In addition, Khriplovich [20] has shown that analogous arguments involving the aforementioned radiative corrections yield limits on T-odd forms of nuclear beta decay constants. From (72) one obtains [31]

$$\mathrm{Im}(C_T + C_T') < 2\times10^{-4};\quad \mathrm{Im}(C_P + C_P') < 0.1\ . \tag{77}$$

Finally, we discuss very briefly the future experimental prospects for d_e. Many proposals for electron EDM experimental searches have been made, among them utilization of certain paramagnetic molecules with large enhancement factors [32,33], and use of laser-cooled atoms in atomic fountains or cells. While each of these proposals has attractive features, each also has its difficulties and uncertainties. On the other hand, we believe that the present experiment can be improved very significantly, and we are now carrying out major modifications, including more efficient detection and use of comparison beams to reduce very significantly the noise and systematic uncertainties arising from the $\mathbf{E}\times\mathbf{v}$ effect, the geometric phase, and leakage and charging currents.

ACKNOWLEDGMENTS

We gratefully acknowledge the collaboration of K. Abdullah, C. Carlberg, and H. Gould in an earlier phase of this experiment. We thank machinist A. Vaynberg, electronics technician P. Miller, and electronics engineer J. Davis for their excellent work; Professor I. B. Khriplovich and Professor M. Suzuki, and Dr. D. Budker for valuable discussions; and R. P. Aditya for technical assistance. This work was supported by the Director, Office of Energy Research, Office of Basic Energy Sciences, Chemical Sciences Division of the U.S. Department of Energy, under Contract No. DE-AC03-76SF00098.

[1] K. Abdullah, C. Carlberg, E. D. Commins, H. Gould, and S. B. Ross, Phys. Rev. Lett. **65**, 2347 (1990).

[2] C. Carlberg, K. Abdullah, E. D. Commins, H. Gould, and S. B. Ross, *A New Experimental Limit on the Electric Dipole Moment of the Electron,* Proceedings of the Twelfth International Conference on Atomic Physics, Ann Arbor, Michigan, 1990, edited by J. C. Zorn, R. R. Lewis, and M. K. Weiss, AIP Conf. Proc. No. 233 (AIP, New York, 1991), p. 442; E. D. Commins, *Search for the Electron Electric Dipole Moment in Atomic Thallium,* Proceedings of Time Reversal—The Arthur Rich Memorial Symposium, Ann Arbor, Michigan, 1991, edited by M. Skalsey, P. H. Bucksbaum, R. S. Conti, and D. W. Gidley, AIP Conf. Proc. No. 270 (AIP, New York, 1993), p. 34.

[3] J. P. Carrico, T. S. Stein, E. Lipworth, and M. C. Weisskopf, Phys. Rev. A **1**, 211 (1970).

[4] H. Gould, Phys. Rev. Lett. **24**, 1091 (1970).

[5] M. A. Player and P. G. H. Sandars, J. Phys. B **3**, 1620 (1970).

[6] S. A. Murthy, D. Krause, L. Li, and L. R. Hunter, Phys.

Rev. Lett. **63**, 965 (1989).
[7] K. F. Smith *et al.*, Phys. Lett. B **234**, 191 (1990).
[8] I. S. Altarev *et al.*, Phys. Lett. B **276**, 242 (1992).
[9] D. Cho, K. Sangster, and E. A. Hinds, Phys. Rev. Lett. **63**, 2559 (1989).
[10] J. P. Jacobs, W. M. Klipstein, S. Lamoreaux, B. R. Heckel, and E. N. Fortson, Phys. Rev. Lett. **71**, 3782 (1993).
[11] R. Carosi *et al.*, Phys. Lett. B **237**, 303 (1990).
[12] K. S. Babu and S. M. Barr, Phys. Rev. D **49**, R2156 (1994).
[13] S. M. Barr and G. Segre, Phys. Rev. D **48**, 302 (1993).
[14] S. M. Barr and A. Zee, Phys. Rev. Lett. **65**, 21 (1990); J. G. Gunion and R. Vega, Phys. Lett. B **251**, 157 (1990).
[15] The predictions of various theoretical models of CP violation for the electron EDM are reviewed in W. Bernreuther and M. Suzuki, Rev. Mod. Phys. **63**, 313 (1991); S. M. Barr, Int. J. Mod. Phys. A **8**, 209 (1993).
[16] L. I. Schiff, Phys. Rev. **132**, 2194 (1963).
[17] P. G. H. Sandars, Phys. Lett. **14**, 194 (1965); **22**, 290 (1966).
[18] Z. W. Liu and H. P. Kelly, Phys. Rev. A **45**, R4210 (1992).
[19] V. M. Khatsymovsky, I. B. Khriplovich, and A. S. Yelkhovsky, Ann. Phys. (Paris) **186**, 1 (1988); S. M. Barr, Phys. Rev. Lett. **68**, 1822 (1992); Phys. Rev. D **45**, 4148 (1992).
[20] R. S. Conti and I. B. Khriplovich, Phys. Rev. Lett. **68**, 3262 (1992); I. B. Khriplovich, Nucl. Phys. B **352**, 38 (1991).
[21] N. F. Ramsey, Phys. Rev. **76**, 996 (1949).
[22] N. F. Ramsey, *Molecular Beams* (Oxford University Press, Oxford, 1990), p. 365.
[23] P. Kusch and V. W. Hughes, in *Atomic and Molecular Beam Spectroscopy,* edited by S. Flugge, Handbuch der Physik Vol. XXXVII/1 (Springer, Berlin, 1959), p. 23.
[24] S.B. Ross, J. R. Davis, and J. Dutra, Rev. Sci. Instrum. **64**, 2379 (1993).
[25] E. D. Commins, Am. J. Phys. **59**, 1077 (1991).
[26] H. Gould, Phys. Rev. A **14**, 923 (1976).
[27] R. M. Sternheimer, Phys. Rev. **183**, 112 (1969).
[28] W. R. Johnson, D. S. Guo, M. Idrees, and J. Sapirstein, Phys. Rev. A **34**, 1043 (1986).
[29] A. C. Hartley, E. Lindroth, and A.-M. Martensson-Pendrill, J. Phys. B **23**, 3417 (1990).
[30] V. V. Flambaum and I. B. Khriplovich, Zh. Eksp. Teor. Fiz. **89**, 1505 (1985) [Sov. Phys. JETP **62**, 872 (1985)].
[31] I. B. Khriplovich (private communication).
[32] V. L. Flambaum and I. B. Khriplovich, Phys. Lett. A **110**, 121 (1984).
[33] E. A. Hinds and K. Sangster, *Testing Time Reversal Symmetry with Molecules,* Proceedings of Time Reversal—The Arthur Rich Memorial Symposium, Ann Arbor, Michigan, 1991, edited by M. Skalsey, P. H. Bucksbaum, R. S. Conti, and D. W. Gidley, AIP Conf. Proc. No. 270 (AIP, New York, 1993), p. 77.